A moving grid finite element method applied to a mechanobiochemical model for 3D cell migration

Article (Accepted Version)

A moving grid finite element method applied to a mechanobiochemical model for 3D cell migration.

Laura Murphy, Anotida Madzvamuse[1]

University of Sussex, School of Mathematical and Physical Sciences,
Department of Mathematics,
BN1 9QH, UK

Abstract

This work presents the development, analysis and numerical simulations of a biophysical model for 3D cell deformation and movement, which couples biochemical reactions and biomechanical forces. We propose a mechanobiochemical model which considers the actin filament network as a viscoelastic and contractile gel. The mechanical properties are modelled by a force balancing equation for the displacements, the pressure and contractile forces are driven by actin and myosin dynamics, and these are in turn modelled by a system of reaction-diffusion equations on a moving cell domain. The biophysical model consists of highly non-linear partial differential equations whose analytical solutions are intractable. To obtain approximate solutions to the model system, we employ the moving grid finite element method. The numerical results are supported by linear stability theoretical results close to bifurcation points during the early stages of cell migration. Numerical simulations exhibited show both simple and complex cell deformations in 3-dimensions that include cell expansion, cell protrusion and cell contraction. The computational framework presented here sets a strong foundation that allows to study more complex and experimentally driven reaction-kinetics involving actin, myosin and other molecular species that play an important role in cell movement and deformation.

Keywords: Mechanobiochemical model, viscoelastic, force balance equation, cell motility, moving grid finite elements, reaction-diffusion equations, partial differential equations, moving boundary problem

1. Introduction

Cell movement is critical in multicelluar organisms due to roles in embryogenesis, wound healing, immune response, cancer metastasis, tumour invasion, and other processes, therefore, understanding cell movement is of great importance to medicine and to understanding our origins [13, 14, 20, 32]. To this end, there are numerous recent studies concerning the migration of single and cell populations and as well as tumour growth some of which couple biochemical models to biomechanical processes [67]. For example, competition population models such as predator-prey models [17, 29] have been employed to study the effects of stress on tumour mechanics as well as considering competition between healthy and cancer cells. For single cell migration in three dimensions, recent studies have focused, for example, on predicting how cell speed is affected by the levels of adhesion to the extracellular matrix (ECM) as well as how traction forces for amoeboid motility could be provided by steric interactions between the cell and the ECM [79, 84]. Adaptability of migration modes was recently explored computationally by use of a discrete model in [85]. They found that, by varying the adhesions, locations of protrusion and contraction, and including or excluding degradation of the ECM, the model reproduces six distinct modes of motility which have been observed experimentally. Such discrete models could be coupled in parallel with continuous 3D models such as the one proposed in this study.

Numerous advanced nonlinear mechanical/statistical models exist in the literature focusing on different biochemical processes and biomechanical properties linking tissue dynamics to single cell behaviour [30, 29]. For example, the work in [30] considers an elemental nonlinear elastic model of adherent cells to study the influence of prestress

[1]Corresponding author: a.madzvamuse@sussex.ac.uk

and number of cytoskeleton filaments on single-cell stiffness within the framework of a pseudo-stationary anchored cell. In [29] a multiscale poroelastic model is coupled to an ecological model to describe competition between health and abnormal cancer cells. To understand the roles of mechanical stiffness and transient active force generation behaviour when a cell undergoes cyclic loading, the work in [54] presents a thermodynamic cross-bridge cycling model to describe the interactions between actin-myosin dynamics with stress fibres. Other models in the literature consider the effect of external factors, such as cyclic compression [54], ultrasound frequencies [30] and substrate compliance [23], on the cell's internal stress fibres. Cells can also propel themselves using the beating or rotation of a flagellum, hence 3D kinematics models have been developed from 2D images in [68]. Although aforementioned work focus on nonlinear mechanics, in the absence of detailed experimental observations, we focus solely on a linear mechanical model and leave work on nonlinear for future studies.

Mechanical forces and reaction-diffusion systems on evolving surfaces are in important part of many cell motility models [15, 27, 59]. These models are demonstrations of non-adhesion driven motility and numerical simulations successfully imitated features of both directed pseudopod-driven migration due to an external chemoattractant [27, 59] and motility through a porous medium [15]. Unlike the model proposed in this study, these works do not include any protein interactions in the bulk (cytosol) of the cell.

Our study focuses on how cytosol cellular biochemical interactions inside the cell coupled with the cytosol biomechanical properties affect cell movement in three dimensions without any external extracellular matrix cues nor interactions with other cells nor the environment (i.e. cell migration through complex environments for example). In [25], actin simply pushes on the membrane, the created protrusion force is likely to be confined to the periphery of the cell [75]. In other models, including our current model, actin is also involved in generating contractile stresses and flows [34, 44, 77]. There is experimental evidence to suggest that the concentration of myosin linearly affects the stress [38, 41, 70, 75, 81] or similarly the rate of contraction [58, 8]. The concentration of myosin and the stress forces in the cell have a positive feedback on each other, when attached to fixed point myosin induces movement of the membrane, conversely, myosin responds to membrane tension [2].

In this study we consider a mechanobiochemical model previously studied by George et al. [35, 34, 52] which we will extend to 3-dimensions as well as introducing for the first time, the role of myosin in the modelling and computational framework. The model comprises of a system of reaction-diffusion equations for cellular proteins and a linear viscoelastic mechanical model for cell movement and deformation. Given that the model is highly nonlinear, exact analytical solutions are not possible to obtain in closed form, instead, we will seek to compute numerical approximations to these exact solutions. Numerical methods abound for solving complex partial differential equation (PDEs), methods that have been employed to model cell motility include finite differences, phase field methods, boundary element methods (BEM), immersed boundary methods, level set methods (LSM), [3, 11, 59, 63, 77, 78, 80] and arbitrary Lagrangian-Eulerian methods [46]. Choosing a suitable method for a particular model is a balance between the ease of application within the model's framework and the reliability of solutions produced. Finite differences were used in previous incarnations of the model [3, 77]. This method is very useful and easy to implement on fixed and simple domains but it is significantly more complicated to incorporate for the evolving domains and surfaces we wish to use and there are often problems with a moving boundary. Level set methods are used extensively in cell simulations and are useful when cells split and reconnect, therefore, it may be advantageous to use this method in the future when considering cell proliferation (cell division) and apoptosis (cell death) [82]. In this work we are not concerned with cells splitting.

The finite element method is well known to easily handle complex and evolving cellular domains and can be generalised to multidimensions with little complications, hence it is the ideal method to numerically solve our model system. Finite element methods have been widely used to model cell motility [10, 12, 19, 27, 37, 46, 53, 69, 73, 79], and can be implemented in diverse ways depending on the model. Given these considerations we develop a finite element based formulation which follows the work of George [34] with the extension into multidimensions which involve solving two reaction-diffusion equations corresponding to actin and myosin concentrations. Additionally we develop our numerical solver based on *deal.ii* [6] rather than ALBERTA as previously done by George [34].

This article is therefore structured as follows: In Section 2, we introduce the mechanobiochemical model. Theoretical predictions of the spatiotemporal behaviour of the solutions of the model close to bifurcation points are presented in Appendix A, these identify important bifurcation parameters which are used in the numerical simulations of the full model. In Section 3, theoretical predictions are used to validate finite element simulations since there are no analytical solutions to compare with. Far away from bifurcation points, finite element simulations illustrating 3D cell

movement and deformation are exhibited in Section 4. We conclude and discuss the key findings of our study and its applicability to cell migration and also elucidate model limitations that underpin our future studies in Section 5.

2. A mechanobiochemical model

The model we consider and extend is inspired by contractile models of the actin cytogel [44, 62]. These models comprise of a force balance equation modelling the displacements of the cell when deformed and a single reaction-diffusion equation for the concentration of the gel that in turn drives cell movement. The idea of pressure-driven protrusion and the use of concentration of actin originates from Alt and Tranquillo [3]. In their model they assume movement is produced by a balance between contractile force of the actin network pulling on the membrane and pressure pushing on the membrane. This was extended by Stephanou et al. so that large deformations could be modelled which is more realistic for most cells [77]. George further extended this model by observing (and hence modelling) that higher actin concentration in a region leads to more pressure [34]. In the previous models a polar coordinate system was used and radial extension of the cell was calculated [3, 77]. Unlike this approach, we follow the work of George and study the mechanobiochemical model in its physical Cartesian coordinates without any need for coordinate transformation [34]. We extend the work by George in two key ways, first by extending from two, to three dimensions and second by adding the consideration of the concentration of myosin. We hypothetically model the concentrations of, and interactions between, actin and myosin using two reaction-diffusion equations. The reaction-diffusion equations are coupled to a force balance equation which describes the movement of the cell. The model equations are outlined as follows.

We assume that the cell shape is a simply connected and continuously deforming domain: $\boldsymbol{\Omega}_t \subset \mathbb{R}^3$ with boundary $\partial\boldsymbol{\Omega}_t$, where $t \in I = [0, T_f]$, $T_f > 0$. Any point $\mathbf{x} \in \boldsymbol{\Omega}_t$ is defined by $\mathbf{x} = (x(t), y(t), z(t))$. The domain, its boundary and their evolution are unknown quantities which must be solved for all time t as part of the numerical solution procedure. We define the displacement of $\mathbf{x}$ at time t by $\mathbf{u} = (u(\mathbf{x}(t), t), v(\mathbf{x}(t), t), w(\mathbf{x}(t), t))^T$. For simplicity, we adopt a Lagrangian formulation where we assume that the rate of change of the displacements generate the flow velocity $\boldsymbol{\beta}$, i.e. $\frac{d\mathbf{u}}{dt} = \boldsymbol{\beta}$, which drives the spatiotemporal dynamics of the molecular species. We will also define $\boldsymbol{\omega}_n$ to represent the normal velocity of the boundary. Let us consider two unknown molecular species where we assume the concentration of F-actin, and bound myosin, at point $\mathbf{x}(t)$ are given by $a = a(\mathbf{x}(t), t)$, and $m = m(\mathbf{x}(t), t)$ respectively. Then the mechanobiochemical model describing the dynamics of the actin network is given by the following dimensional system of the equations,

$$\nabla \cdot (\boldsymbol{\sigma}_v + \boldsymbol{\sigma}_e + \boldsymbol{\sigma}_c + \boldsymbol{\sigma}_p) = \mathbf{0} \qquad \text{in } \boldsymbol{\Omega}_t, t \in I, \tag{1a}$$

$$\frac{\partial a}{\partial t} + \nabla \cdot (a\boldsymbol{\beta}) - D_a \Delta a - f(a, m) = 0 \qquad \text{in } \boldsymbol{\Omega}_t, t \in I, \tag{1b}$$

$$\frac{\partial m}{\partial t} + \nabla \cdot (m\boldsymbol{\beta}) - D_m \Delta m - g(a, m) = 0 \qquad \text{in } \boldsymbol{\Omega}_t, t \in I, \tag{1c}$$

$$a(\mathbf{x}(t), t) = a_0, \quad \mathbf{u}(\mathbf{x}(t), t) = \mathbf{0} \qquad \text{for } \mathbf{x} \in \boldsymbol{\Omega}_0, \tag{1d}$$

$$\boldsymbol{\beta} = \boldsymbol{\omega}_n \qquad \text{for } \mathbf{x} \in \partial\boldsymbol{\Omega}_t, t \in I, \tag{1e}$$

$$\boldsymbol{\sigma}_v \cdot \mathbf{n} = \boldsymbol{\sigma}_e \cdot \mathbf{n} = \mathbf{n} \cdot \nabla a = \mathbf{n} \cdot \nabla m = 0 \qquad \text{for } \mathbf{x} \in \partial\boldsymbol{\Omega}_t, t \in I, \tag{1f}$$

where the stress tensors are given by:

- viscous $\boldsymbol{\sigma}_v(\mathbf{u}) = \mu_1 \frac{\partial \boldsymbol{\varepsilon}}{\partial t} + \mu_2 \frac{\partial \phi}{\partial t}\mathbf{I}$ where μ_1 and μ_2 are shear and bulk viscosities respectively, $\boldsymbol{\varepsilon}$ is the the strain tensor ($\frac{1}{2}(\nabla\mathbf{u} + \nabla\mathbf{u}^T)$) and ϕ is the dilation ($\nabla \cdot \mathbf{u}$) [9, 24, 83].
- elastic $\boldsymbol{\sigma}_e(\mathbf{u}) = \frac{E}{1+\nu}(\boldsymbol{\varepsilon} + \frac{\nu}{1-2\nu}\phi\mathbf{I})$ where E is the Youngs modulus and ν is the Poisson ratio [9, 24, 83].
- contractile $\boldsymbol{\sigma}_c(a, m) = (\psi a^2 e^{-a/a_{sat}} + cm)\mathbf{I}$, where ψ and c are the contractility coefficients for a and m, respectively, and a_{sat} is the saturation coefficient of actin. The first term is the same as in [34] and we have added that the contractile force is linearly proportional to the concentration of myosin as suggested by experimental observations [8, 38, 41, 58, 70, 75, 81]. Similarly, there is experimental evidence to suggest that the concentration of myosin linearly affects the stress [38, 41, 70, 75, 81] or similarly the rate of change in contraction [58, 8].

- pressure $\boldsymbol{\sigma}_p(\mathbf{u}, a) = \dfrac{p}{1+\phi}(1 + \frac{2}{\pi}\delta(l)\arctan a)\mathbf{I}$ [77]. This describes two types of pressure. The first term describes the hydrostatic pressure that is present everywhere and corresponds to the osmotic pressure in the cell which depends on the dilation ϕ and pressure coefficient p. The second term models the fact that close to the membrane there is polymerisation pressure caused by the polymerising actin filaments pushing on the cell membrane. This increases with increasing concentration of filaments a and we choose the initial state of this concentration to be resident close to the membrane, i.e. in a region less than 20% of the cell radius from the edge. To define this region we use $\delta(l)$ and the points $\boldsymbol{\xi} = (\xi_x, \xi_y, \xi_z) \in \boldsymbol{\Omega}_0$. There exists a family of bijective mappings between the initial and current domains, we can let $l : \boldsymbol{\Omega}_t \times I \to \mathbb{R}$ and correspondingly $\hat{l} : \boldsymbol{\Omega}_0 \times I \to [0, 1]$ then $\hat{l}(\boldsymbol{\xi}, t) = l(\mathbf{x}(\boldsymbol{\xi}, t), t)$. Hence, we calculate the distance from the centroid by

$$\delta(l) = \begin{cases} 1, & \text{if } \sqrt{\xi_x^2 + \xi_y^2 + \xi_z^2} > 0.8, \\ 0, & \text{otherwise.} \end{cases} \tag{2}$$

In the reaction-diffusion equations we have assumed constant diffusion coefficients for actin and myosin, and these are given D_a and D_m respectively. In the above notation, $\Delta = \frac{\partial^2}{\partial x^2} + \frac{\partial^2}{\partial y^2} + \frac{\partial^2}{\partial z^2}$ denotes the Laplace operator in three dimensions. On the boundary, we assume continuity between the flow velocity and the normal velocity of the boundary, i.e. that $\boldsymbol{\beta} = \omega_n$[1, 50, 51]. The interactions between actin and myosin are described by the reaction terms $f(a, m)$ and $g(a, m)$ respectively. We have formulated different plausible reaction kinetics in the absence of experimental data and for the sake of brevity, in this work, we only present one such model. For further details, we refer the interested reader to consult [57]. Although we will discuss the implementation of one specific plausible model, other models can be easily incorporated and studied in a similar fashion. For illustrative purposes we consider the following hypothetical reaction kinetics

$$f(a, m) = k_a(a_c - a) + k_{am}\frac{a^2(m_c - m)}{1 + Ka^2}, \tag{3a}$$

$$g(a, m) = -k_{ma}(a_c - a) - k_{am}\frac{a^2(m_c - m)}{1 + Ka^2}, \tag{3b}$$

where we begin with the same reaction term, $k_a(a_c - a)$, as used in [35, 34, 52]. k_a is the rate of polymerisation/depolymerisation and a_c is the equilibrium concentration and if the concentration is above this critical value then F-actin will depolymerise at the same rate. Next, since myosin binds to actin the amount of myosin will increase due to higher concentration of actin, hence the term $-k_{ma}(a_c - a)$ where k_{ma} is the rate of binding/unbinding of myosin. Defining m_c as the unstable equilibrium concentration of m, the last term in the actin equation represents that actin will depolymerise with higher concentrations of myosin and is subject to a saturation coefficient K, for a. The negation is true for myosin since myosin is seen to accumulate.

We assume the initial shape is a stationary unit sphere and the initial conditions for actin and myosin densities are a small perturbation from the homogeneous steady state (when $m = m_c = a = a_c = 1$). Thus we have three connected equations: the solutions to (1b) (actin concentration) and (1c) (myosin concentration) affect the contractile and pressure parts of the force balance equation and the solution to (1a) (displacement) affects the reaction-diffusion equations through the convection terms and the changing shape of the domain.

2.1. Summary of results from linear stability theory

We employ linear stability theory to identify key parameters and compute analytical solutions close to bifurcation points. Close to bifurcation points, we will use the linear stability analytical results to validate the numerical solver of our full mechanobiochemical model that we will use to find approximate solutions to the model problem given that no analytical solutions can be obtained for the full model. This approach is a generalisation of the method for the mechanobiochemical model described in [35] for the case of two dimensions where only one reaction-diffusion equation was considered. In Appendix A we see that parameters, in particular ψ and c, can be varied so that particular patterns become unstable and grow. These patterns correspond to eigenfunctions of the Laplacian on the chosen volume, and are illustrated in Figure 1. In other words, in the early stages of movement, plots of the magnitude of the displacement and concentrations will look qualitatively similar to particular eigenfunctions. In Appendix A, for analytical purposes we study the non-dimensionalised system while for the moving grid finite element implementation we work with the full dimensional model.

	Description	Form / Value	Reference
$a(\mathbf{x}(t),t)$	actin	concentration	Unknown
$m(\mathbf{x}(t),t)$	myosin	concentration	Unknown
$\boldsymbol{\varepsilon}$	strain tensor	$\frac{1}{2}(\nabla\mathbf{u}+\nabla\mathbf{u}^T)$	
ϕ	dilation	$\nabla\cdot\mathbf{u}$	
$\boldsymbol{\beta}$	flow velocity	$\frac{\partial\mathbf{u}}{\partial t}$	Unknown
ω_n	normal velocity of boundary		
μ_1	shear viscosity	$96.15\frac{dyn\cdot s}{cm^2}$	[7]
μ_2	bulk viscosity	$250\frac{dyn\cdot s}{cm^2}$	[7]
E	Young's modulus	$1.5\frac{dyn\cdot s}{cm^2}$	Estimated [34]
ν	Poisson ratio	0.3	Estimated [34]
D_a	diffusion coefficient	$0.012\frac{cm^2}{s}$	[77]
D_a	diffusion coefficient	$0.003\frac{cm^2}{s}$	Estimated
a_c	conc. at equilibrium	$1\frac{mol}{cm^3}$ normalised	Derived in [34]
m_c	conc. at equilibrium	$1\frac{mol}{cm^3}$ normalised	Derived from model
a_{sat}	saturation conc.	$1.4\frac{mol}{cm^3}$ normalised	[77]
l_0	vicinity of the membrane	80% of cell radius	Estimated [34]
ψ	contractility coefficient for actin	70	
c	contractility coefficient for myosin	10	
p	pressure coefficient	1.7	

Table 1: Descriptions of parameters. The contractility coefficients (ψ and c), and reaction constants (k_a, k_{ma} and k_{am}) are also estimated by use of linear stability theory (see Appendix A for details).

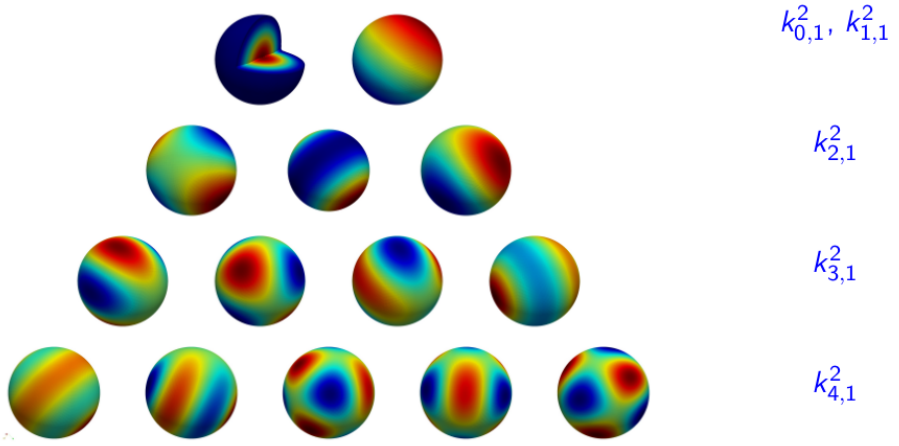

Figure 1: Analytical solutions to the eigenvalue problem on the unit sphere i.e. (A.6) for selected values of l,m,n. For $l \geq 1$ there are multiple eigenfunctions for each eigenvalue. (Colour version online).

3. Finite element formulation

We have formulated a very complex non-linear system of partial differential equations. It is not possible to analytically solve this system, therefore we must turn to numerical methods to find approximate solutions. Previous numerical solution methods of earlier models were represented in a polar coordinate system and solved using finite differences [3, 77]. A moving grid finite element method was developed by George [35] for the case of two dimensions and the numerical solver was developed in an alternative finite element software package known as ALBERTA. Here, we generalise this numerical approach to 3-dimensions where we implement the numerical solver in *deal.ii*. Specifically, we employ the moving grid finite element method [5, 47, 49, 52] to compute approximate numerical solutions of the coupled viscoelastic reaction-diffusion system defined in 3D Cartesian coordinate system. Unlike the full compact spatial Laplace operator notation employed for the linear stability analytical study in Appendix A for the mechanobiochemical model, we instead opt to use the vector-matrix component which lends itself amenable to the finite element weak formulation. A compact notation could also be used but at the expense of not being able to deal with individual components which is crucial for the method.

To begin, the force balance is separated into a system of three partial differential equations representing the three space dimensions. This clarifies the derivation of the weak formulation. Since $\boldsymbol{\sigma}_v, \boldsymbol{\sigma}_e, \boldsymbol{\sigma}_c$ and $\boldsymbol{\sigma}_p$ (as described in Section 2) are all stress tensors we can write them in matrix form. In three dimensions, strain and dilation are given by

$$\epsilon(\mathbf{u}) := \frac{1}{2}(\nabla\mathbf{u} + (\nabla\mathbf{u})^T) = \begin{pmatrix} \frac{\partial u}{\partial x} & \frac{1}{2}(\frac{\partial v}{\partial x} + \frac{\partial u}{\partial y}) & \frac{1}{2}(\frac{\partial u}{\partial z} + \frac{\partial w}{\partial x}) \\ \frac{1}{2}(\frac{\partial v}{\partial x} + \frac{\partial u}{\partial y}) & \frac{\partial v}{\partial y} & \frac{1}{2}(\frac{\partial v}{\partial z} + \frac{\partial w}{\partial y}) \\ \frac{1}{2}(\frac{\partial v}{\partial x} + \frac{\partial u}{\partial y}) & \frac{1}{2}(\frac{\partial w}{\partial y} + \frac{\partial v}{\partial z}) & \frac{\partial w}{\partial z} \end{pmatrix} \quad \text{and} \quad \phi(\mathbf{u}) := \frac{\partial u}{\partial x} + \frac{\partial v}{\partial y} + \frac{\partial w}{\partial z}, \tag{4a}$$

respectively. It follows then that we can write the stress tensors in three-dimensional tensor-matrix form:

$$\boldsymbol{\sigma}_v = \begin{pmatrix} \mu_{1+2}\frac{\partial \dot{u}}{\partial x} + \mu_2(\frac{\partial \dot{v}}{\partial y} + \frac{\partial \dot{w}}{\partial z}) & \frac{\mu_1}{2}(\frac{\partial \dot{v}}{\partial x} + \frac{\partial \dot{u}}{\partial y}) & \frac{\mu_1}{2}(\frac{\partial \dot{w}}{\partial x} + \frac{\partial \dot{u}}{\partial z}) \\ \frac{\mu_1}{2}(\frac{\partial \dot{v}}{\partial x} + \frac{\partial \dot{u}}{\partial y}) & \mu_2(\frac{\partial \dot{u}}{\partial x} + \frac{\partial \dot{w}}{\partial z}) + \mu_{1+2}\frac{\partial \dot{v}}{\partial y} & \frac{\mu_1}{2}(\frac{\partial \dot{v}}{\partial z} + \frac{\partial \dot{w}}{\partial y}) \\ \frac{\mu_1}{2}(\frac{\partial \dot{w}}{\partial x} + \frac{\partial \dot{u}}{\partial z}) & \frac{\mu_1}{2}(\frac{\partial \dot{v}}{\partial z} + \frac{\partial \dot{w}}{\partial y}) & \mu_{1+2}\frac{\partial \dot{w}}{\partial z} + \mu_2(\frac{\partial \dot{u}}{\partial x} + \frac{\partial \dot{v}}{\partial y}) \end{pmatrix},$$

$$\boldsymbol{\sigma}_e = \frac{E}{1+\nu}\begin{pmatrix} \frac{\partial u}{\partial x} + \nu'\phi(\mathbf{u}) & \frac{1}{2}(\frac{\partial v}{\partial x} + \frac{\partial u}{\partial y}) & \frac{1}{2}(\frac{\partial u}{\partial z} + \frac{\partial w}{\partial x}) \\ \frac{1}{2}(\frac{\partial v}{\partial x} + \frac{\partial u}{\partial y}) & \frac{\partial v}{\partial y} + \nu'\phi(\mathbf{u}) & \frac{1}{2}(\frac{\partial v}{\partial z} + \frac{\partial w}{\partial y}) \\ \frac{1}{2}(\frac{\partial w}{\partial x} + \frac{\partial u}{\partial z}) & \frac{1}{2}(\frac{\partial v}{\partial z} + \frac{\partial w}{\partial y}) & \frac{\partial w}{\partial z} + \nu'\phi(\mathbf{u}) \end{pmatrix},$$

$$\boldsymbol{\sigma}_c = \begin{pmatrix} \psi a^2 e^{-a/a_{sat}} + cm & 0 & 0 \\ 0 & \psi a^2 e^{-a/a_{sat}} + cm & 0 \\ 0 & 0 & \psi a^2 e^{-a/a_{sat}} + cm \end{pmatrix},$$

$$\boldsymbol{\sigma}_p = \begin{pmatrix} \frac{p}{1+\phi}\left(1 + \frac{2}{\pi}\delta(l)\tan^{-1}a\right) & 0 & 0 \\ 0 & \frac{p}{1+\phi}\left(1 + \frac{2}{\pi}\delta(l)\tan^{-1}a\right) & 0 \\ 0 & 0 & \frac{p}{1+\phi}\left(1 + \frac{2}{\pi}\delta(l)\tan^{-1}a\right) \end{pmatrix},$$

where $\mu_{1+2} = \mu_1 + \mu_2$ and $\nu' = \nu/(1-2\nu)$. Substituting these expressions into $\nabla \cdot (\boldsymbol{\sigma}_v + \boldsymbol{\sigma}_e + \boldsymbol{\sigma}_c + \boldsymbol{\sigma}_p) = \mathbf{0}$ gives us

three equations

$$\frac{\partial}{\partial x}\left(D_{11}\frac{\partial \dot{u}}{\partial x}+D_{12}\left(\frac{\partial \dot{v}}{\partial y}+\frac{\partial \dot{w}}{\partial z}\right)+C_{11}\frac{\partial u}{\partial x}+C_{12}\left(\frac{\partial v}{\partial y}+\frac{\partial w}{\partial z}\right)\right)$$
$$+\frac{\partial}{\partial y}\left(D_{33}\left(\frac{\partial \dot{v}}{\partial x}+\frac{\partial \dot{u}}{\partial y}\right)+C_{33}\left(\frac{\partial v}{\partial x}+\frac{\partial u}{\partial y}\right)\right)+\frac{\partial}{\partial z}\left(D_{33}\left(\frac{\partial \dot{w}}{\partial x}+\frac{\partial \dot{u}}{\partial z}\right)+C_{33}\left(\frac{\partial w}{\partial x}+\frac{\partial u}{\partial z}\right)\right)=-\frac{\partial f_1}{\partial x},$$

$$\frac{\partial}{\partial x}\left(D_{33}\left(\frac{\partial \dot{v}}{\partial x}+\frac{\partial \dot{u}}{\partial y}\right)+C_{33}\left(\frac{\partial v}{\partial x}+\frac{\partial u}{\partial y}\right)\right)+\frac{\partial}{\partial y}\left(D_{11}\frac{\partial \dot{v}}{\partial y}+D_{12}\left(\frac{\partial \dot{u}}{\partial x}+\frac{\partial \dot{w}}{\partial z}\right)\right.$$
$$\left.+C_{11}\frac{\partial v}{\partial y}+C_{12}\left(\frac{\partial u}{\partial x}+\frac{\partial w}{\partial z}\right)\right)+\frac{\partial}{\partial z}\left(D_{33}\left(\frac{\partial \dot{w}}{\partial y}+\frac{\partial \dot{w}}{\partial z}\right)+C_{33}\left(\frac{\partial w}{\partial z}+\frac{\partial v}{\partial z}\right)\right)=-\frac{\partial f_2}{\partial y},$$

$$\frac{\partial}{\partial x}\left(D_{33}\left(\frac{\partial \dot{w}}{\partial x}+\frac{\partial \dot{u}}{\partial z}\right)+C_{33}\left(\frac{\partial w}{\partial x}+\frac{\partial u}{\partial z}\right)\right)+\frac{\partial}{\partial y}\left(D_{33}\left(\frac{\partial \dot{v}}{\partial z}+\frac{\partial \dot{w}}{\partial y}\right)+C_{33}\left(\frac{\partial v}{\partial z}+\frac{\partial w}{\partial y}\right)\right)$$
$$+\frac{\partial}{\partial z}\left(D_{11}\frac{\partial \dot{w}}{\partial z}+D_{12}\left(\frac{\partial \dot{v}}{\partial y}+\frac{\partial \dot{u}}{\partial x}\right)+C_{11}\frac{\partial w}{\partial z}+C_{12}\left(\frac{\partial u}{\partial x}+\frac{\partial v}{\partial y}\right)\right)=-\frac{\partial f_3}{\partial z},$$

where

$$f_1=f_2=f_3=\left[\frac{p}{1+\phi}\left(1+\frac{2}{\pi}\delta(l)\arctan a\right)+\psi a^2 e^{-a/a_{sat}}+cm\right], \tag{7a}$$

$$D_{11}=\mu_1+\mu_2,\quad D_{12}=\mu_2,\quad D_{33}=\frac{\mu_1}{2}, \tag{7b}$$

$$C_{11}=\frac{E(1-\nu)}{(1+\nu)(1-2\nu)},\quad C_{12}=\frac{E\nu}{(1+\nu)(1-2\nu)}\text{ and }C_{33}=\frac{E}{2(1+\nu)}. \tag{7c}$$

3.1. Weak formulation

To find the weak formulation, we multiply by a space-time-dependent test function $\hat{\phi}(\mathbf{x},t)\in H^1(\mathbf{\Omega}_t)$, where $H^1(\mathbf{\Omega}_t)$ is the Sobolev space of L^2 functions over Ω_t with weak derivative in L^2, and integrate over the domain. This takes into account Green's formula and the boundary conditions. The boundary condition $\boldsymbol{\sigma}_v\cdot\mathbf{n}=\boldsymbol{\sigma}_e\cdot\mathbf{n}=0$ means that boundary term disappears during integration. The weak formulation is to find $u(\mathbf{x},t)$, $v(\mathbf{x},t)$ and $w(\mathbf{x},t)\in H^1(\mathbf{\Omega}_t)$, $t\in I$ such that

$$\int_{\mathbf{\Omega}_t}\frac{\partial\hat{\phi}}{\partial x}\left(D_{11}\frac{\partial \dot{u}}{\partial x}+D_{12}\left(\frac{\partial \dot{v}}{\partial y}+\frac{\partial \dot{w}}{\partial z}\right)+C_{11}\frac{\partial u}{\partial x}+C_{12}\left(\frac{\partial v}{\partial y}+\frac{\partial w}{\partial z}\right)\right)+\frac{\partial\hat{\phi}}{\partial y}\left(D_{33}\left(\frac{\partial \dot{v}}{\partial x}+\frac{\partial \dot{u}}{\partial y}\right)\right.$$
$$\left.+C_{33}\left(\frac{\partial v}{\partial x}+\frac{\partial u}{\partial y}\right)\right)+\frac{\partial\hat{\phi}}{\partial z}\left(D_{33}\left(\frac{\partial \dot{w}}{\partial x}+\frac{\partial \dot{u}}{\partial z}\right)+C_{33}\left(\frac{\partial w}{\partial x}+\frac{\partial u}{\partial z}\right)\right)d\mathbf{\Omega}_t=-\int_{\mathbf{\Omega}_t}\frac{\partial\hat{\phi}}{\partial x}f_1 d\mathbf{\Omega}_t+\int_{\partial\mathbf{\Omega}_t}\hat{\phi}f_1 n_1 ds,$$

$$\int_{\mathbf{\Omega}_t}\frac{\partial\hat{\phi}}{\partial x}\left(D_{33}\left(\frac{\partial \dot{v}}{\partial x}+\frac{\partial \dot{u}}{\partial y}\right)+C_{33}\left(\frac{\partial v}{\partial x}+\frac{\partial u}{\partial y}\right)\right)+\frac{\partial\hat{\phi}}{\partial y}\left(D_{11}\frac{\partial \dot{v}}{\partial y}+D_{12}\left(\frac{\partial \dot{u}}{\partial x}+\frac{\partial \dot{w}}{\partial z}\right)\right.$$
$$\left.+C_{11}\frac{\partial v}{\partial y}+C_{12}\left(\frac{\partial u}{\partial x}+\frac{\partial w}{\partial z}\right)\right)+\frac{\partial\hat{\phi}}{\partial z}\left(D_{33}\left(\frac{\partial \dot{w}}{\partial y}+\frac{\partial \dot{w}}{\partial z}\right)+C_{33}\left(\frac{\partial w}{\partial z}+\frac{\partial v}{\partial z}\right)\right)d\mathbf{\Omega}_t=-\int_{\mathbf{\Omega}_t}\frac{\partial\hat{\phi}}{\partial y}f_2 d\mathbf{\Omega}_t+\int_{\partial\mathbf{\Omega}_t}\hat{\phi}f_2 n_2 ds,$$

$$\int_{\mathbf{\Omega}_t}\frac{\partial\hat{\phi}}{\partial x}\left(D_{33}\left(\frac{\partial \dot{w}}{\partial x}+\frac{\partial \dot{u}}{\partial z}\right)+C_{33}\left(\frac{\partial w}{\partial x}+\frac{\partial u}{\partial z}\right)\right)+\frac{\partial\hat{\phi}}{\partial y}\left(D_{33}\left(\frac{\partial \dot{v}}{\partial z}+\frac{\partial \dot{w}}{\partial y}\right)+C_{33}\left(\frac{\partial v}{\partial z}+\frac{\partial w}{\partial y}\right)\right)$$
$$+\frac{\partial\hat{\phi}}{\partial z}\left(D_{11}\frac{\partial \dot{w}}{\partial z}+D_{12}\left(\frac{\partial \dot{v}}{\partial y}+\frac{\partial \dot{u}}{\partial x}\right)+C_{11}\frac{\partial w}{\partial z}+C_{12}\left(\frac{\partial u}{\partial x}+\frac{\partial v}{\partial y}\right)\right)d\mathbf{\Omega}_t=-\int_{\mathbf{\Omega}_t}\frac{\partial\hat{\phi}}{\partial z}f_3 d\mathbf{\Omega}_t+\int_{\partial\mathbf{\Omega}_t}\hat{\phi}f_3 n_3 ds.$$

Since $\frac{\partial f_1}{\partial x}$, $\frac{\partial f_2}{\partial y}$ and $\frac{\partial f_3}{\partial z}$ are functions of the unknown solution variables $a(\mathbf{x}, t)$ and $m(\mathbf{x}, t)$, these become extremely challenging to integrate analytically. To avoid computing these patial derivatives, we have used identities derived from the Gradient Theorem to re-write the weak formulation in a tractable form as demonstrated above. In other words we have used the identity

$$\int_{\mathbf{\Omega}_t} \frac{\partial f_j}{\partial x} \hat{\phi} d\mathbf{\Omega}_t = -\int_{\mathbf{\Omega}_t} \frac{\partial \hat{\phi}}{\partial x} f_j d\mathbf{\Omega}_t + \int_{\partial \mathbf{\Omega}_t} \hat{\phi} f_j n_j ds, \tag{9}$$

for $j = 1, 2, 3$, where x can also be substituted by y and z. n_1, n_2, n_3 are the direction cosines of the outward unit vector $\mathbf{n}$ normal to $\partial \mathbf{\Omega}_t$.

Next we want to find the weak formulation of the reaction-diffusion equations which is defined as

$$\frac{\partial a}{\partial t} + \nabla \cdot (a\boldsymbol{\beta}) - D_a \Delta a = f(a, m), \quad \frac{\partial m}{\partial t} + \nabla \cdot (m\boldsymbol{\beta}) - D_m \Delta m = g(a, m). \tag{10}$$

To proceed, we exploit knowledge about the model formulation for reaction-diffusion systems on evolving domains (as well as on surfaces) and by using appropriate results from the Reynolds Transport Theorem, to apply the product rule and convert to the material derivative (defined as $\frac{Da}{Dt} = \frac{\partial a}{\partial t} + a(\nabla \cdot \boldsymbol{\beta})$, in [66]) to obtain the following

$$\begin{aligned} \frac{Da}{Dt} - D_a \Delta a + a(\nabla \cdot \boldsymbol{\beta}) &= f(a, m), \\ \frac{Dm}{Dt} - D_m \Delta m + m(\nabla \cdot \boldsymbol{\beta}) &= g(a, m). \end{aligned}$$

Now continuing as with the force balance equation, we multiply by a space-time-dependent test function $\hat{\psi}(\mathbf{x}, t) \in H^1(\mathbf{\Omega}_t)$ and integrate over the domain. The terms $(D_a \Delta a)\hat{\psi}$ and $(D_m \Delta m)\hat{\psi}$ can be simplified using the Divergence Theorem and the remaining part of the left hand side we use the Reynolds Transport Theorem. This means the weak formulation can be written as: Find $a(\mathbf{x}, t)$, $m(\mathbf{x}, t) \in H^1(\mathbf{\Omega}_t), t \in I$ such that

$$\frac{\partial}{\partial t} \int_{\mathbf{\Omega}_t} a\hat{\psi} d\mathbf{\Omega}_t + \int_{\mathbf{\Omega}_t} \left(D_a \nabla a \cdot \nabla \hat{\psi} \right) d\mathbf{\Omega}_t = \int_{\mathbf{\Omega}_t} \left(f(a, m)\hat{\psi} + a \frac{D\hat{\psi}}{Dt} \right) d\mathbf{\Omega}_t, \tag{12a}$$

$$\frac{\partial}{\partial t} \int_{\mathbf{\Omega}_t} m\hat{\psi} d\mathbf{\Omega}_t + \int_{\mathbf{\Omega}_t} \left(D_m \nabla m \cdot \nabla \hat{\psi} \right) d\mathbf{\Omega}_t = \int_{\mathbf{\Omega}_t} \left(g(a, m)\hat{\psi} + m \frac{D\hat{\psi}}{Dt} \right) d\mathbf{\Omega}_t, \tag{12b}$$

for all $\hat{\psi}(\mathbf{x}, t) \in H^1(\mathbf{\Omega}_t)$.

3.2. Space discretisation

We now wish to define the problem at discrete points in space. To do this, we define the computational domain $\Omega_{h,t}$ as a polyhedral approximation to $\mathbf{\Omega}_t$, i.e. $\Omega_{h,t}$ the spatial discretisation of $\mathbf{\Omega}_t$. This discretisation induces quadrilateral meshes on the surface. For a fixed time $t \in I$, let $V_h(t) \subset H^1(\mathbf{\Omega}_t)$ be the space of piecewise linear functions on $\Omega_{h,t}$ defined by

$$V_h(t) := \left\{ \psi \in C^0(\Omega_{h,t}) \;\middle|\; \psi|_z \text{ is linear affine for each } z \in \Omega_{h,t} \right\}.$$

Then we seek to find $u_h(\mathbf{x},t)$, $v_h(\mathbf{x},t)$, $w_h(\mathbf{x},t)$, $a_h(\mathbf{x},t)$, $m_h(\mathbf{x},t) \in V_h(t)$, $t \in I$ such that

$$\int_{\mathbf{\Omega}_{h,t}} \frac{\partial\hat{\phi}}{\partial x}\left(D_{11}\frac{\partial\dot{u}_h}{\partial x} + D_{12}\left(\frac{\partial\dot{v}_h}{\partial y} + \frac{\partial\dot{w}_h}{\partial z}\right) + C_{11}\frac{\partial u_h}{\partial x} + C_{12}\left(\frac{\partial v_h}{\partial y} + \frac{\partial w_h}{\partial z}\right)\right) + \frac{\partial\hat{\phi}}{\partial y}\left(D_{33}\left(\frac{\partial\dot{v}_h}{\partial x} + \frac{\partial\dot{u}_h}{\partial y}\right) + C_{33}\left(\frac{\partial v_h}{\partial x} + \frac{\partial u_h}{\partial y}\right)\right)$$
$$+ \frac{\partial\hat{\phi}}{\partial z}\left(D_{33}\left(\frac{\partial\dot{w}_h}{\partial x} + \frac{\partial\dot{u}_h}{\partial z}\right) + C_{33}\left(\frac{\partial w_h}{\partial x} + \frac{\partial u_h}{\partial z}\right)\right) d\mathbf{\Omega}_t = -\int_{\mathbf{\Omega}_{h,t}} \frac{\partial\hat{\phi}}{\partial x} f_1 d\mathbf{\Omega}_{h,t} + \int_{\partial\mathbf{\Omega}_{h,t}} \hat{\phi} f_1 n_1 ds,$$

$$\int_{\mathbf{\Omega}_{h,t}} \frac{\partial\hat{\phi}}{\partial x}\left(D_{33}\left(\frac{\partial\dot{v}_h}{\partial x} + \frac{\partial\dot{u}_h}{\partial y}\right) + C_{33}\left(\frac{\partial v_h}{\partial x} + \frac{\partial u_h}{\partial y}\right)\right) + \frac{\partial\hat{\phi}}{\partial y}\left(D_{11}\frac{\partial\dot{v}_h}{\partial y} + D_{12}\left(\frac{\partial\dot{u}_h}{\partial x} + \frac{\partial\dot{w}_h}{\partial z}\right) + C_{11}\frac{\partial v_h}{\partial y} + C_{12}\left(\frac{\partial u_h}{\partial x} + \frac{\partial w_h}{\partial z}\right)\right)$$
$$+ \frac{\partial\hat{\phi}}{\partial z}\left(D_{33}\left(\frac{\partial\dot{w}_h}{\partial y} + \frac{\partial\dot{w}_h}{\partial z}\right) + C_{33}\left(\frac{\partial w_h}{\partial z} + \frac{\partial v_h}{\partial z}\right)\right) d\mathbf{\Omega}_{h,t} = -\int_{\mathbf{\Omega}_{h,t}} \frac{\partial\hat{\phi}}{\partial y} f_2 d\mathbf{\Omega}_{h,t} + \int_{\partial\mathbf{\Omega}_{h,t}} \hat{\phi} f_2 n_2 ds,$$

$$\int_{\mathbf{\Omega}_{h,t}} \frac{\partial\hat{\phi}}{\partial x}\left(D_{33}\left(\frac{\partial\dot{w}_h}{\partial x} + \frac{\partial\dot{u}_h}{\partial z}\right) + C_{33}\left(\frac{\partial w_h}{\partial x} + \frac{\partial u_h}{\partial z}\right)\right) + \frac{\partial\hat{\phi}}{\partial y}\left(D_{33}\left(\frac{\partial\dot{v}_h}{\partial z} + \frac{\partial\dot{w}_h}{\partial y}\right) + C_{33}\left(\frac{\partial v_h}{\partial z} + \frac{\partial w_h}{\partial y}\right)\right)$$
$$+ \frac{\partial\hat{\phi}}{\partial z}\left(D_{11}\frac{\partial\dot{w}_h}{\partial z} + D_{12}\left(\frac{\partial\dot{v}_h}{\partial y} + \frac{\partial\dot{u}_h}{\partial x}\right) + C_{11}\frac{\partial w_h}{\partial z} + C_{12}\left(\frac{\partial u_h}{\partial x} + \frac{\partial v_h}{\partial y}\right)\right) d\mathbf{\Omega}_{h,t} = -\int \mathbf{\Omega}_{h,t}\frac{\partial\hat{\phi}}{\partial z} f_3 d\mathbf{\Omega}_{h,t} + \int_{\partial\mathbf{\Omega}_{h,t}} \hat{\phi} f_3 n_3 ds,$$

and

$$\frac{\partial}{\partial t}\int_{\Omega_{h,t}} a_h\hat{\psi} d\Omega_{h,t} + \int_{\Omega_{h,t}} D_a \nabla a_h \cdot \nabla\hat{\psi} d\Omega_{h,t} = \int_{\Omega_{h,t}} \left(I_h f(a_h, m_h)\hat{\psi} + a_h\frac{D\hat{\psi}}{Dt}\right) d\Omega_{h,t},$$
$$\frac{\partial}{\partial t}\int_{\Omega_{h,t}} m_h\hat{\psi} d\Omega_{h,t} + \int_{\Omega_{h,t}} D_m \nabla m_h \cdot \nabla\hat{\psi} d\Omega_{h,t} = \int_{\Omega_{h,t}} \left(I_h g(a_h, m_h)\hat{\psi} + m_h\frac{D\hat{\psi}}{Dt}\right) d\Omega_{h,t},$$

for all $\hat{\phi},\ \hat{\psi} \in V_h(t)$, where I_h is the Lagrange interpolant of f and g onto the finite element space [33]. Let $\{\phi_j\}_{j=1}^{nde}$ be a set of piecewise bilinear shape functions on Ω_h, then this set forms a basis of $V_h(t)$. We can then express u_h, v_h, w_h, a_h and m_h in terms of the bilinear basis functions:

$$u_h = \sum_{j=1}^{nde} U_j\phi_j, \quad v_h = \sum_{j=1}^{nde} V_j\phi_j, \quad w_h = \sum_{j=1}^{nde} W_j\phi_j, \quad a_h = \sum_{j=1}^{nde} \alpha_j\phi_j \quad \text{and} \quad m_h = \sum_{j=1}^{nde} \mu_j\phi_j. \tag{15}$$

This means that we are left with equations which contain only simple functions and their derivatives and point values for the variables. Substituting u_h, v_h, and w_h into the above equations and using the Galerkin formulation, take the test functions to belong the same spaces as the nodal basis functions. Hence, the force balance equations can be written in block matrix-vector form

$$\begin{bmatrix} \mathbf{A}^{11} & \mathbf{A}^{12} & \mathbf{A}^{13} \\ [\mathbf{A}^{12}]^T & \mathbf{A}^{22} & \mathbf{A}^{23} \\ [\mathbf{A}^{13}]^T & [\mathbf{A}^{23}]^T & \mathbf{A}^{33} \end{bmatrix} \begin{Bmatrix} \frac{d\mathbf{U}}{dt} \\ \frac{d\mathbf{V}}{dt} \\ \frac{d\mathbf{W}}{dt} \end{Bmatrix} + \begin{bmatrix} \mathbf{B}^{11} & \mathbf{B}^{12} & \mathbf{B}^{13} \\ [\mathbf{B}^{12}]^T & \mathbf{B}^{22} & \mathbf{B}^{23} \\ [\mathbf{B}^{13}]^T & [\mathbf{B}^{23}]^T & \mathbf{B}^{33} \end{bmatrix} \begin{Bmatrix} \mathbf{U} \\ \mathbf{V} \\ \mathbf{W} \end{Bmatrix} = \begin{Bmatrix} \mathbf{F}^1 \\ \mathbf{F}^2 \\ \mathbf{F}^3 \end{Bmatrix}, \tag{16}$$

where $\{\mathbf{U}(t)\} = (U_1, ..., U_{nde})$, $\{\mathbf{V}(t)\} = (V_1, ..., V_{nde})$, $\{\mathbf{W}(t)\} = (W_1, ..., W_{nde})$ and:

$$\mathbf{A}^{11}_{ij}(t) := \int_{\mathbf{\Omega}_{h,t}} D_{11}\frac{\partial\phi_i}{\partial x}\frac{\partial\phi_j}{\partial x} + D_{33}\left(\frac{\partial\phi_i}{\partial y}\frac{\partial\phi_j}{\partial y} + \frac{\partial\phi_i}{\partial z}\frac{\partial\phi_j}{\partial z}\right)d\mathbf{\Omega}_{h,t},$$

$$\mathbf{A}^{22}_{ij}(t) := \int_{\mathbf{\Omega}_{h,t}} D_{33}\left(\frac{\partial\phi_i}{\partial x}\frac{\partial\phi_j}{\partial x} + \frac{\partial\phi_i}{\partial z}\frac{\partial\phi_j}{\partial z}\right) + D_{11}\frac{\partial\phi_i}{\partial y}\frac{\partial\phi_j}{\partial y}d\mathbf{\Omega}_{h,t},$$

$$\mathbf{A}^{33}_{ij}(t) := \int_{\mathbf{\Omega}_{h,t}} D_{33}\left(\frac{\partial\phi_i}{\partial x}\frac{\partial\phi_j}{\partial x} + \frac{\partial\phi_i}{\partial y}\frac{\partial\phi_j}{\partial y}\right) + D_{11}\frac{\partial\phi_i}{\partial z}\frac{\partial\phi_j}{\partial z}d\mathbf{\Omega}_{h,t},$$

$$\mathbf{B}^{11}_{ij}(t) := \int_{\mathbf{\Omega}_{h,t}} C_{11}\frac{\partial\phi_i}{\partial x}\frac{\partial\phi_j}{\partial x} + C_{33}\left(\frac{\partial\phi_i}{\partial y}\frac{\partial\phi_j}{\partial y} + \frac{\partial\phi_i}{\partial z}\frac{\partial\phi_j}{\partial z}\right)d\mathbf{\Omega}_{h,t},$$

$$\mathbf{B}^{22}_{ij}(t) := \int_{\mathbf{\Omega}_{h,t}} C_{33}\left(\frac{\partial\phi_i}{\partial x}\frac{\partial\phi_j}{\partial x} + \frac{\partial\phi_i}{\partial z}\frac{\partial\phi_j}{\partial z}\right) + C_{11}\frac{\partial\phi_i}{\partial y}\frac{\partial\phi_j}{\partial y}d\mathbf{\Omega}_{h,t},$$

$$\mathbf{B}^{33}_{ij}(t) := \int_{\mathbf{\Omega}_{h,t}} C_{33}\left(\frac{\partial\phi_i}{\partial x}\frac{\partial\phi_j}{\partial x} + \frac{\partial\phi_i}{\partial y}\frac{\partial\phi_j}{\partial y}\right) + C_{11}\frac{\partial\phi_i}{\partial z}\frac{\partial\phi_j}{\partial z}d\mathbf{\Omega}_{h,t},$$

$$\mathbf{A}^{12}_{ij}(t) := \int_{\mathbf{\Omega}_{h,t}} D_{12}\frac{\partial\phi_i}{\partial x}\frac{\partial\phi_j}{\partial y} + D_{33}\frac{\partial\phi_i}{\partial y}\frac{\partial\phi_j}{\partial x}d\mathbf{\Omega}_{h,t}, \quad \mathbf{A}^{13}_{ij}(t) := \int_{\mathbf{\Omega}_{h,t}} D_{12}\frac{\partial\phi_i}{\partial x}\frac{\partial\phi_j}{\partial z} + D_{33}\frac{\partial\phi_i}{\partial z}\frac{\partial\phi_j}{\partial x}d\mathbf{\Omega}_{h,t},$$

$$\mathbf{A}^{23}_{ij}(t) := \int_{\mathbf{\Omega}_{h,t}} D_{12}\frac{\partial\phi_i}{\partial y}\frac{\partial\phi_j}{\partial z} + D_{33}\frac{\partial\phi_i}{\partial z}\frac{\partial\phi_j}{\partial y}d\mathbf{\Omega}_{h,t}, \quad \mathbf{B}^{12}_{ij}(t) := \int_{\mathbf{\Omega}_{h,t}} C_{12}\frac{\partial\phi_i}{\partial x}\frac{\partial\phi_j}{\partial y} + C_{33}\frac{\partial\phi_i}{\partial y}\frac{\partial\phi_j}{\partial x}d\mathbf{\Omega}_{h,t},$$

$$\mathbf{B}^{13}_{ij}(t) := \int_{\mathbf{\Omega}_{h,t}} C_{12}\frac{\partial\phi_i}{\partial x}\frac{\partial\phi_j}{\partial z} + C_{33}\frac{\partial\phi_i}{\partial z}\frac{\partial\phi_j}{\partial x}d\mathbf{\Omega}_{h,t}, \quad \mathbf{B}^{23}_{ij}(t) := \int_{\mathbf{\Omega}_{h,t}} C_{12}\frac{\partial\phi_i}{\partial y}\frac{\partial\phi_j}{\partial z} + C_{33}\frac{\partial\phi_i}{\partial z}\frac{\partial\phi_j}{\partial y}d\mathbf{\Omega}_{h,t},$$

$$\mathbf{F}^1_j(t) := -\int_{\Omega_{h,t}} f_1\frac{\partial\phi_j}{\partial x}d\Omega_{h,t} + \int_{\partial\Omega_{h,t}} n_1 f_1\phi_j ds, \qquad \mathbf{F}^2_j(t) := -\int_{\Omega_{h,t}} f_2\frac{\partial\phi_j}{\partial y}d\Omega_{h,t} + \int_{\partial\Omega_{h,t}} n_2 f_2\phi_j ds,$$

$$\mathbf{F}^3_j(t) := -\int_{\Omega_{h,t}} f_3\frac{\partial\phi_j}{\partial z}d\Omega_{h,t} + \int_{\partial\Omega_{h,t}} n_3 f_3\phi_j ds.$$

It must be noted that in the above we have used the fact that $\hat{\phi} \in V_h(t)$ and $\hat{\psi} \in V_h(t)$. For the sake of ease of notation and computation we define the following block matrices and vectors

$$[\mathbf{A}] := \begin{bmatrix} \mathbf{A}^{11} & \mathbf{A}^{12} & \mathbf{A}^{13} \\ [\mathbf{A}^{12}]^T & \mathbf{A}^{22} & \mathbf{A}^{23} \\ [\mathbf{A}^{13}]^T & [\mathbf{A}^{23}]^T & \mathbf{A}^{33} \end{bmatrix}, \; [\mathbf{B}] := \begin{bmatrix} \mathbf{B}^{11} & \mathbf{B}^{12} & \mathbf{B}^{13} \\ [\mathbf{B}^{12}]^T & \mathbf{B}^{22} & \mathbf{B}^{23} \\ [\mathbf{B}^{13}]^T & [\mathbf{B}^{23}]^T & \mathbf{B}^{33} \end{bmatrix}, \; \{\mathbf{U}\} := \begin{Bmatrix} \mathbf{U} \\ \mathbf{V} \\ \mathbf{W} \end{Bmatrix} \text{ and } \{\mathbf{F}\} := \begin{Bmatrix} \mathbf{F}^1 \\ \mathbf{F}^2 \\ \mathbf{F}^3 \end{Bmatrix}. \tag{18a}$$

Therefore the force balance equation's semi-discrete finite element formulation can be written compactly as

$$[\mathbf{A}]\frac{\{d\mathbf{U}\}}{dt} + [\mathbf{B}]\{\mathbf{U}\} = \{\mathbf{F}\}. \tag{19}$$

The same is done for the reaction-diffusion equations, and we additionally use the transport property of basis functions, (space discretisation means that the material derivative of basis functions $\frac{D\hat{\psi}}{Dt} = 0$) which is demonstrated in [26] and [34]. Considering the reaction kinetics to be as in Eqs (3), (see Section 2), we can write the reaction-diffusion equations in semi-discrete form

$$\frac{\partial}{\partial t}(\mathbf{M}\boldsymbol{\alpha}) + D_a\mathbf{K}\boldsymbol{\alpha} = k_a a_c\mathbf{H} - k_a\mathbf{M}\boldsymbol{\alpha} + k_{am}\mathbf{M}\frac{\boldsymbol{\alpha}(1-\boldsymbol{\mu})}{1+K\boldsymbol{\alpha}^2}, \tag{20a}$$

$$\frac{\partial}{\partial t}(\mathbf{M}\boldsymbol{\mu}) + D_m\mathbf{K}\boldsymbol{\mu} = -k_{ma}a_c\mathbf{H} + k_{ma}\mathbf{M}\boldsymbol{\alpha} - k_{am}\mathbf{M}\frac{\boldsymbol{\alpha}(1-\boldsymbol{\mu})}{1+K\boldsymbol{\alpha}^2}, \tag{20b}$$

where vector operations in $\boldsymbol{\alpha}(1-\boldsymbol{\mu})/(1+K\boldsymbol{\alpha}^2)$ are pointwise and

$$M_{i,j} = \int_{\Omega_{h,t}} \phi_i\phi_j, \quad K_{i,j} = \int_{\Omega_{h,t}} \nabla\phi_i \cdot \nabla\phi_j \quad \text{and} \quad H_j = \int_{\Omega_{h,t}} \phi_j. \tag{21}$$

In the case where exact integrations are not possible, Gauss numerical quadrature is employed to compute the integrals [64]. These are all computed in the deal.II implementation [6]. An alternative approach is to use mass-lumping [18, 33, 45] for the finite element method to speed up the computational time required to assemble the matrices and this forms part of our future studies.

3.3. Time discretisation

Next we carry out the temporal discretisation of the system of ordinary differential equations arising from the finite element discretisation. To proceed, we split the interval into a finite number of sub-intervals $[t^n, t^{n+1}]$ and use a uniform time step $\Delta t := t^{n+1} - t^n$. We then use an implicit-explicit (IMEX) finite differentiation formula [43, 47, 71] to obtain the fully discrete algebraic system of linear equations. The IMEX scheme treats fully implicitly the diffusion part, while the nonlinear reaction terms are treated fully explicitly. This avoids computing the Jacobian matrix associated with fully implicit schemes for reaction kinetics and therefore requires only evaluations of the reaction kinetics. We also remark that an adaptive timestepping scheme could also be employed to speed up computations, but this was not undertaken in this study. Thus the fully discrete problem now reads

$$([\mathbf{A}]^n + \Delta t[\mathbf{B}]^n)\,\mathbf{U}^{n+1} = [\mathbf{A}]^n\{\mathbf{U}\}^n + \Delta t\{\mathbf{F}\}^n, \tag{22a}$$

$$\left[\mathbf{M}^{n+1} + \Delta t D_a \mathbf{K}^{n+1}\right]\boldsymbol{\alpha}^{n+1} = \mathbf{M}^n\boldsymbol{\alpha}^n + \Delta t(k_a(a_c\mathbf{H}^n - \mathbf{M}^n\boldsymbol{\alpha}^n) + k_{am}\mathbf{M}^n\frac{\boldsymbol{\alpha}^n(1-\boldsymbol{\mu}^n)}{1+K(\boldsymbol{\alpha}^n)^2}), \tag{22b}$$

$$[\mathbf{M}^{n+1} + \Delta t D_m \mathbf{K}^{n+1}]\boldsymbol{\mu}^{n+1} = \mathbf{M}^n\boldsymbol{\mu}^n + \Delta t(-k_{ma}(a_c\mathbf{H}^n - \mathbf{M}^n\boldsymbol{\alpha}^n) - k_{am}\mathbf{M}^n\frac{\boldsymbol{\alpha}^n(1-\boldsymbol{\mu}^n)}{1+K(\boldsymbol{\alpha}^n)^2}), \tag{22c}$$

where the superscripts ^{n} and $^{n+1}$ are the computed values on the mesh at times t^n and t^{n+1} respectively. Note that we have treated some parts implicitly (e.g. diffusion) and other parts fully explicit (e.g. reactions).

Hence we have three equations all with the same form. At each time-step we assemble the matrices to obtain a system of linear algebraic equations. When solving (22a) we see that the block matrix on the left hand side is not symmetric therefore we use the most effective solver for this which is GMRES [72]. Equations (22b) and (22c) are solved using the conjugate gradient method [40].

3.4. Nodal displacements

The displacement of the nodes of the mesh is chosen to be equal to the flow velocity therefore $\boldsymbol{\beta} := \frac{\partial \mathbf{U}}{\partial t}$. Since $t^{n+1} = t^n + \Delta t$ and $\mathbf{x}(t^n) \in \boldsymbol{\Omega}_{t^n}, \mathbf{x}(t^{n+1}) \in \boldsymbol{\Omega}_{t^{n+1}}$ be points in the respective domains. We can define a first order linear approximation of the flow velocity as:

$$\boldsymbol{\beta}(\mathbf{x}, t^n) = \frac{\mathbf{x}(t^{n+1}) - \mathbf{x}(t^n)}{\Delta t}. \tag{23}$$

This means we can define a new approximation to the domain $\boldsymbol{\Omega}_{t^{n+1}}$ such that

$$\mathbf{x}(t^{n+1}) = \mathbf{x}(t^n) + \Delta t\boldsymbol{\beta}(\mathbf{x}, t^n). \tag{24}$$

At each step we have a new mesh with new shape functions so we must assemble new matrices $\mathbf{M}^n, \mathbf{H}^n, \mathbf{A}^n, \mathbf{B}^n, \mathbf{F}^n$ to iteratively solve the discrete coupled problem as outlined in the following algorithm.

3.5. Numerical algorithm

The fully discrete problem is solved iteratively with the following algorithm:

- Initialise $\mathbf{U}^0$, $\boldsymbol{\alpha}^0$, $\boldsymbol{\mu}^0$ and fixed parameters
- WHILE $t <$ *endtime*
  - Assemble $\mathbf{M}^n, \mathbf{H}^n, \mathbf{A}^n, \mathbf{B}^n, \mathbf{F}^n$
  - Solve for $\mathbf{U}^{n+1}$ using (22a)
  - Compute the new domain using $\mathbf{U}^{n+1}$
  - Solve for $\boldsymbol{\alpha}^{n+1}$ and $\boldsymbol{\mu}^{n+1}$ using (22b) and (22c)

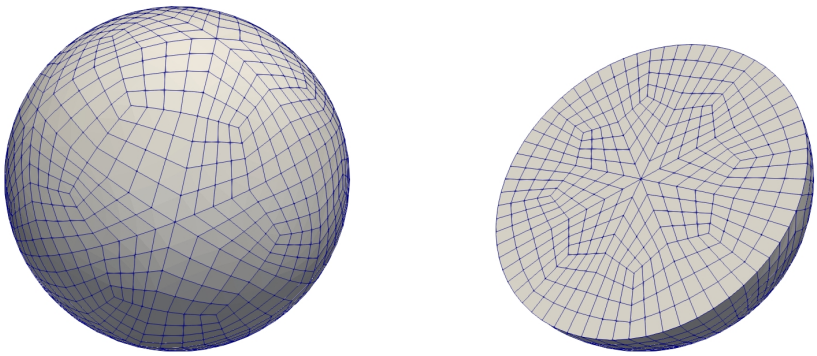

(a) surface (b) cut to show inside

Figure 2: An illustration of the finite element mesh used in the numerical simulations.

- $t = t + \Delta t$

- END

We create a mesh using Gmsh [36], (see Figure 2) and implement this algorithm using deal.II [6], a C++ software library which provides tools to solve partial differential equations which are discretised with finite element methods. Unlike the majority of other finite element software, deal.II uses hexahedral and quadrilateral elements rather than triangular elements.

4. Numerical simulations

Next we present numerical simulations of the full mechanobiochemical model. We want to see the organisation of the molecular species into regions which will cause the cell to move. This organisation may be caused by diffusion-driven instability, or due to the movement of the cell combined with the reaction-diffusion equations. The linear stability analysis of Appendix A holds true for $0 < t << 1$ since geometrical deformation of the cell from the unit sphere (Ω_0) is negligible. In [56] mode isolation and numerical convergence of reaction-diffusion equations were established for the case of a stationary sphere, i.e. in the absence of the force balance mechanical model. The inclusion of the force balance equation for cell deformation entails that more complex stability conditions are obtained, however, establishing numerical convergence for the full model remains an open problem. Nevertheless, it is still possible to choose parameters so that particular modes can be selected during the initial stages of cell deformation. When we consider longer time, and therefore far away from equilibrium, linear stability theory no longer holds making it again impossible to validate numerical results at longer timescales. To provide o confidence in the numerical simulations, global mesh and timestep refinement has been carried out and in the process refinement has given rise to more accurate smooth solutions at the expense of a significant increase in computational time (see Figures 4 and 5 for illustrative purposes). Numerical simulations of the full model far away from bifurcation points reveal some interesting dynamics, we can see, for example, significant protrusions and contractions which deform the cell into many different shapes. Parameters used are shown in Table 2. Initial conditions for actin and myosin are prescribed depending on which eigenmode we wish to excite but are always a small perturbation from the steady state ($a = m = 1$) and include the variable $ran(x)$ which denotes a randomly generated number between 0 and 0.1. It is well known that initial conditions play a crucial role for reaction-diffusion models on stationary and growing domains [47]. For the numerical parameters we take the time step $\Delta t = 10^{-3}$ and the finite element mesh with 8192 active cells and 27123 degrees of freedom. We exploit the implicitly defined mesh regularity measures defined in the software *deal.ii* whereby the numerical is terminated when the mesh regularity measure (Delaunay triangulation criteria) is close to being violated [6, 26]. Hence, there is not precise stopping time, stopping the numerical simulation is subject to the measure index on the

mesh regularity being met. We do not employ any mesh refinement, which might required if one is to deal with longtime dynamics with large deformations in the mesh.

4.1. Excitation of mode $w^1_{1,1}$

In this example, the actin and myosin concentration solutions will be the negation of each other with actin concentration highest on one side and myosin concentration highest on the opposite side. This mode is the first eigenfunction that one might hope to see for the organisation of actin and myosin in a cell because it is similar to what is often observed in a moving cell [21, 58]. $k^2_{1,1} = 2.0816$ is also the lowest eigenvalue. Choosing parameters $\psi = 20$, $c = -80$, $k_a = 0.04$, $k_{ma} = 0.05$ and $k_{am} = 0.06$ and initial conditions

$$a(\mathbf{x}, 0) = 1 + w^1_{1,1}(\mathbf{x}) \times ran(x), \quad m(\mathbf{x}, 0) = 1 - w^1_{1,1}(\mathbf{x}) \times ran(x),$$

we observe that the mode $w^1_{1,1}$ is selected for actin and myosin. In Figure 3 we plot the concentrations of actin and myosin at time $t = 1$. We clearly observe re-polarisation of the cell through symmetry breaking of the concentrations of the molecular species from their almost uniform distribution to a patterned state. Blue indicates where the concentration is low (myosin), while red indicates where the concentration is high (actin). In this case very little cell deformation is observed, rather, the cell is translating as well as expanding in volume. It must be noted however, that the cell has a well defined "front" (defined by high actin concentrations) and "back" (defined by low myosin concentrations), resonating with similar work on cell polarisation [22, 42].

4.2. Cell deformation when $w^0_{2,1}$ is excited initially

The simple first mode is not the only organisation which makes sense or shows similarities to organisation seen in cells. The cell can protrude in more than one direction because of spatio-temporal organisation of the molecular species which satisfy a reaction-diffusion system known to give rise to pattern formation. Depending on the emerging spatial pattern, actin and myosin give rise to the formation of pseudopods through expansion and contraction of the cell. Hence, we continue to isolate other modes to investigate the spatiotemporal organisation of actin and myosin during cell migration. It must be noted that both the parameters, and the initial conditions, play a key role on which modes will grow. The first large cell deformation is seen when choosing initial conditions

$$a(\mathbf{x}, 0) = 1 + w^0_{2,1}(\mathbf{x}) \times ran(x), \quad m(\mathbf{x}, 0) = 1 - w^0_{2,1}(\mathbf{x}) \times ran(x).$$

In Figure 4 we plot the concentrations of actin and myosin and the displacement $\left(|\mathbf{U}| = \sqrt{U^2 + V^2 + W^2}\right)$. The cell expands at the two ends where actin concentration is high (leading to positive curvature in the cell surface) and contracts in the middle where myosin concentration is high (leading to negative curvature in the cell surface). These results are qualitatively similar to the results obtained by [34] in the absence of myosin, one difference being that there is only a very small volume increase because the cell is contracting in the middle as well as protruding. Other results (not shown) when the excited mode for myosin is the same as the mode for actin are very similar to results from the previous model in [57]. In Figure 5 we plot three results for the actin concentration for different timestep and mesh refinements. We obtain identical results to those shown in Figure 4 (last row for actin concentration) confirming the robustness of the numerical solver for different timestep and mesh sizes. Next, we investigate whether more interesting dynamics may occur if we try to excite differing modes for the two concentrations.

4.3. Cell deformation when $w^1_{1,1}$ and $w^0_{2,1}$ are excited for actin and myosin, respectively

While the idea that actin and myosin accumulate in opposite sides is quite well founded, their concentration gradients are rarely exactly opposite. Therefore here we investigate if differing modes can be excited for actin and myosin. Choosing appropriate initial conditions, to encourage different modes to grow, we observe more irregular large cell deformations. In Figure 6 we plot the concentrations of actin and myosin and the displacement when the initial conditions are

$$a(\mathbf{x}, 0) = 1 + w^1_{1,1}(\mathbf{x}) \times ran(x), \quad m(\mathbf{x}, 0) = 1 + w^0_{2,1}(\mathbf{x}) \times ran(x).$$

The cell squeezes where there is high myosin concentration and there is protrusion in the direction of higher actin concentration. This is also illustrated in Figure 7 where the minimum and maximum in each spatial direction are plotted. We again observe that the cell exhibits both positive and negative curvatures of the surface depending on the level of concentration of the respective molecular species.

4.4. Cell deformation when $w^0_{2,1}$ and $w^0_{1,1}$ are excited for actin and myosin, respectively

Let us consider the initial conditions

$$a(\mathbf{x}, 0) = 1 + w^0_{2,1} \times ran(x), \quad m(\mathbf{x}, 0) = 1 + w^0_{1,1}(\mathbf{x}) \times ran(x),$$

that contain the same two eigenfunctions as the last example but with different orientations, ($w^0_{1,1}$ is a rotation of $w^1_{1,1}$). In Figure 8, we illustrate different cell deformation pathways resulting from picking these type of initial conditions and parameters. There is high actin concentration at the top and bottom of the sphere. Without the effect of myosin one would expect the cell to extend in both directions in the same way as in Section 4.2, however there is high myosin concentration at the bottom so the cell only protrudes upwards. Then at $t = 5$ the protrusion slows and there is contraction at the bottom where myosin concentration is high. This is then followed by a subsequent expansion and contraction with the actin and myosin concentrations reorganising to be higher nearer the surface except when the cell is contracting, as shown in Figure 9. Figure 10a shows the change in length in the z-direction while Figure 10b shows the translation of the cell corresponding to the cell deformation pathway of this example.

4.5. Cell deformation when $w^0_{1,1}$ and $w^0_{3,1}$ are excited for actin and myosin, respectively

Next, we begin with initial conditions

$$a(\mathbf{x}, 0) = 1 + w^1_{1,1}(\mathbf{x}) \times ran(x), \quad m(\mathbf{x}, 0) = 1 + w^0_{3,1}(\mathbf{x}) \times ran(x).$$

These lead to a protrusion in the area with highest actin concentration which is pulling the cell in the negative z-direction. At the same time there is inward movement in areas of high myosin concentration, leading to negative curvature. The cell has translated in the negative z-direction and this is plotted in Figure 11, and the translation and change in volume is illustrated in Figure 12.

4.6. Cell deformation when $w^1_{1,1}$ and $w^0_{4,1}$ are excited for actin and myosin, respectively

In another example of mixed modes, we start with

$$a(\mathbf{x}, 0) = 1 + w^1_{1,1}(\mathbf{x}) \times ran(x), \quad m(\mathbf{x}, 0) = 1 + w^0_{4,1}(\mathbf{x}) \times ran(x).$$

These initial conditions lead to cell expansion as shown in Figure 13. The cell contracts inwards at areas of high myosin concentration and protrudes in the remaining areas. There are large protrusions in two opposing directions, the largest being in the direction where actin was initially highest. Subsequently, actin concentrates in areas of high curvature and leading to further protrusion. We observe in this example, the formation of pseudopods which have been well studied in cell migration [27, 59].

Section	4.2	4.3	4.4	4.5	4.6
Figure	4	6	8	11	13
ψ	200	20	150	100	100
c	-40	-80	-40	-80	-100
k_a	0.04	0.4	0.04	0.4	0.09
k_{ma}	0.05	0.5	0.05	0.05	0.09
k_{am}	0.06	0.12	0.06	0.07	0.15

Table 2: Parameters for simulations in the numerical section.

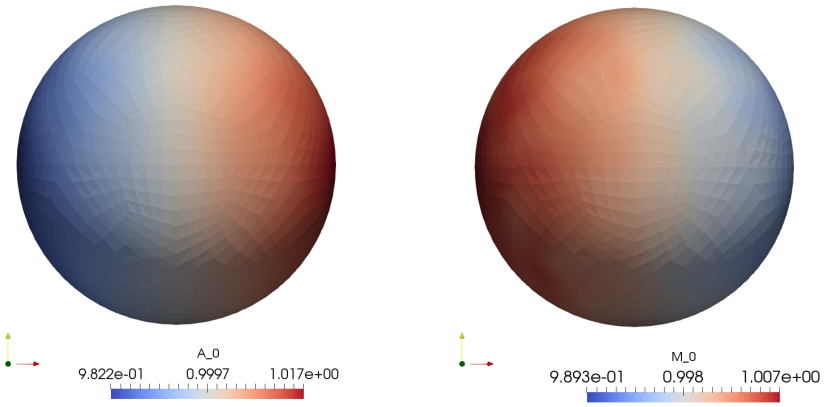

Figure 3: Section 4.1, mode $w^1_{1,1}$. Snaphshots of the numerical solutions for actin $a(x,t)$, myosin $m(x,t)$ at time $t = 1$. These are numerical solutions to the full system (1) using the finite element formulation. (Colour version online).

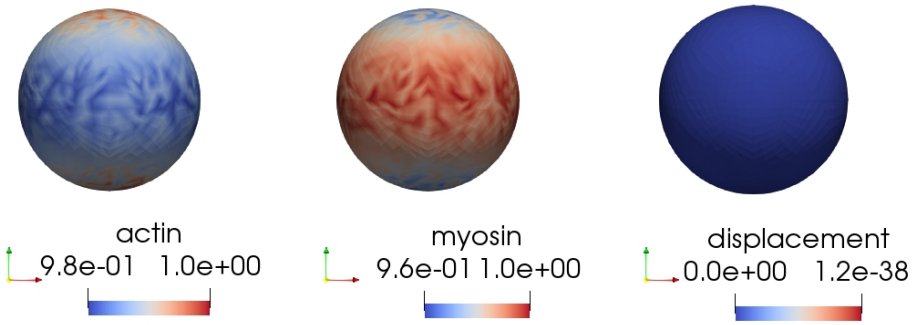

(a) t=0

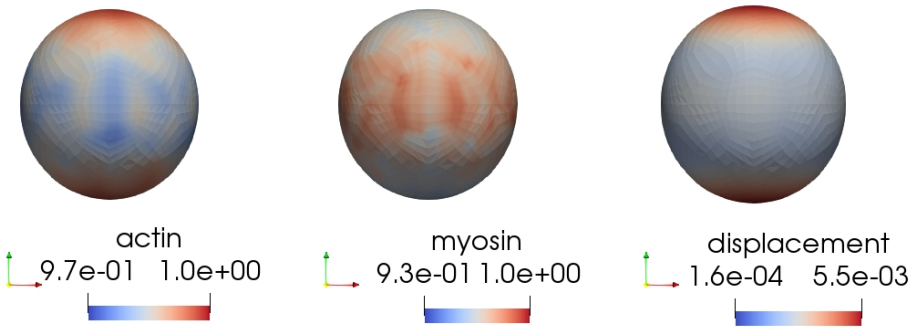

(b) t=1

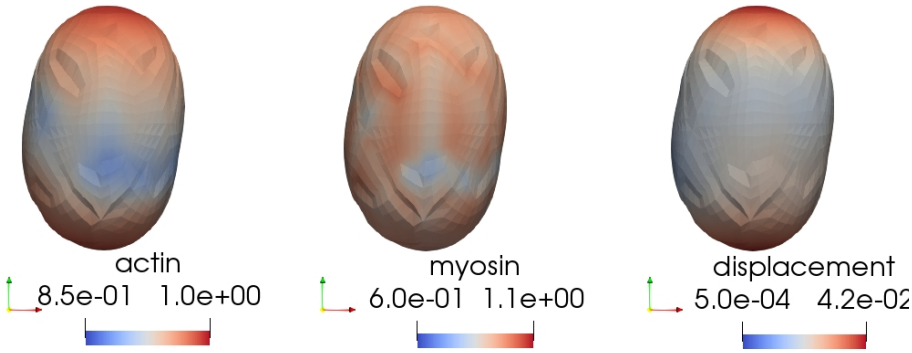

(c) t=6.3

Figure 4: Section 4.2, mode $w^0_{2,1}$. Snaphshots of the numerical solutions for actin $a(x,t)$, myosin $m(x,t)$ and displacement $u(x,t)$ at times $t = 0, 1, 6.3$. There is high actin at two ends, and high myosin in the middle. We then see in (c) that the cell squeezes in the middle stretches in the two directions of higher actin. (Colour version online).

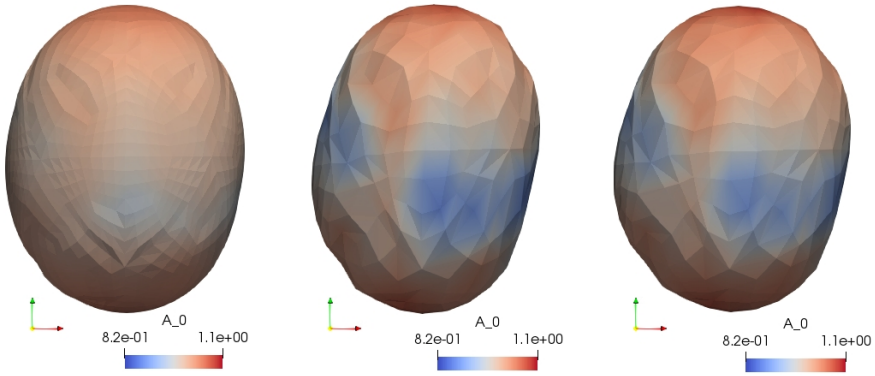

Figure 5: In this plot, we illustrate mesh and timestep refinements by simulating the model equations with identical parameters as in Figure 4 but for different mesh and timesteps. The numerical results show only the actin solution of the mechanobiochemical model at the final time. The results are all obtained at $t = 4$. First figure on the left is the original plot as in Fig 4 obtained with a very refined mesh, second is with a coarser mesh but same time step, and the third is the coarser mesh with half the time step. Refining yields more accurate smooth solutions as expected. (Colour version online).

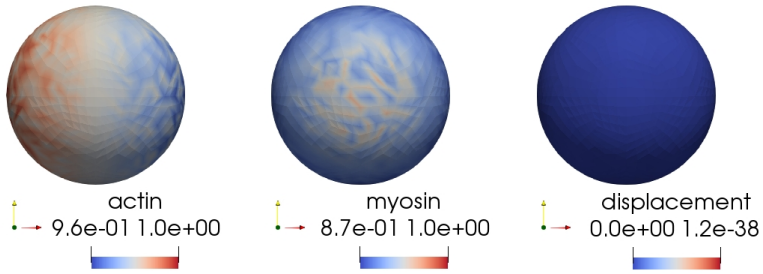

(a) t=0

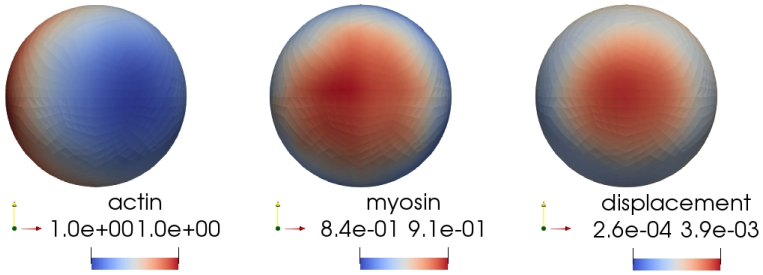

(b) t=1

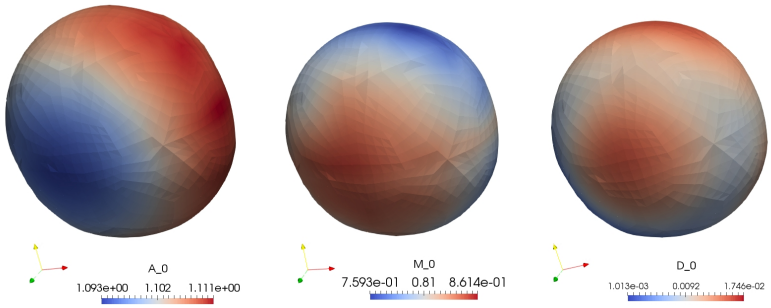

(c) t=9

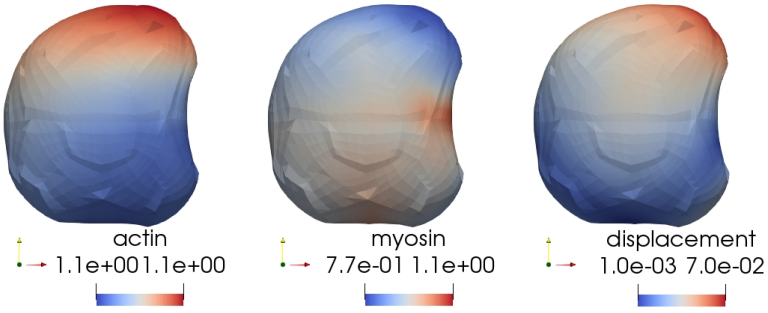

(d) t=13

Figure 6: Section 4.3, modes $w^1_{1,1}$ and $w^0_{2,1}$. Snaphshots of the numerical solutions for actin $a(x,t)$, myosin $m(x,t)$ and displacement $u(x,t)$ at times $t = 0, 1, 9, 13$. The sphere is squeezed where there is high myosin and then there is a protrusion in the area of high actin. Displacements in the x, y and z directions are shown in Figure 7. (Colour version online).

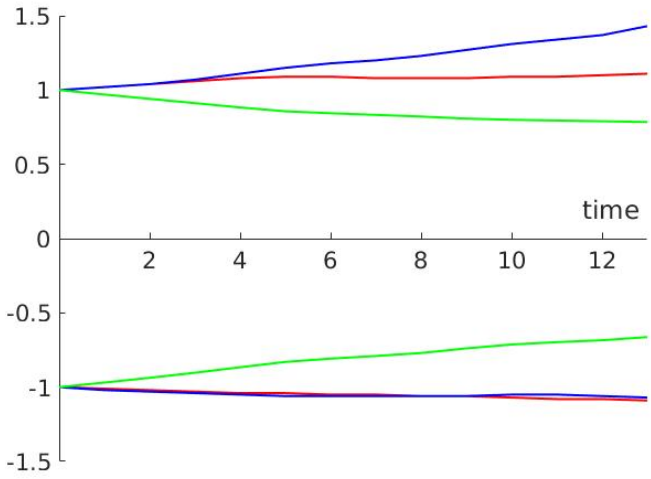

Figure 7: Plot to show the minimum and maximum of x (red), y (blue) and z (green), i.e. the the boundary of the cell in the different directions, for the example in Section 4.3 and Figure 6. The cell is contracting in the y direction, expanding slightly in the x direction but significantly in the positive z-direction. (Colour version online).

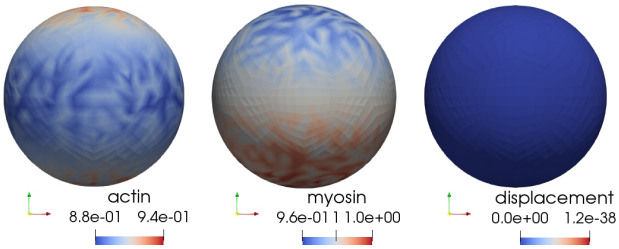

(a) t=0

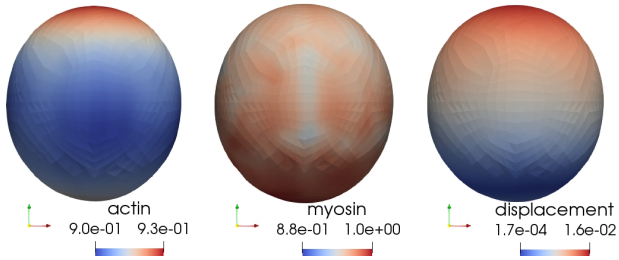

(b) t=5

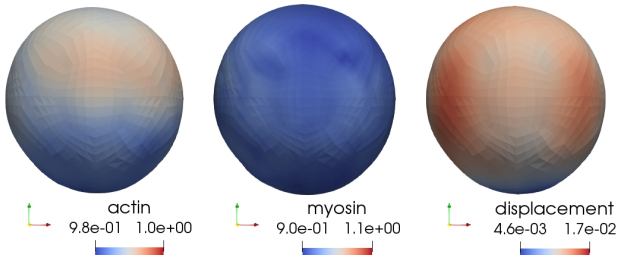

(c) t=20

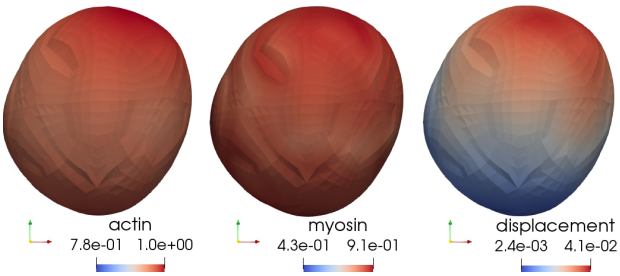

(d) t=29

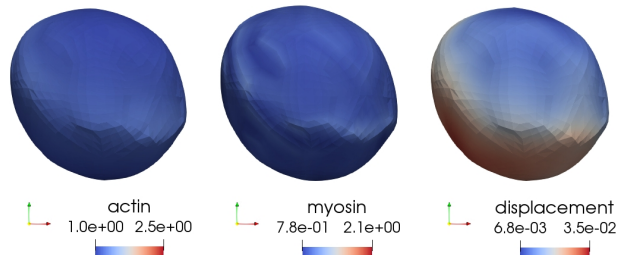

(e) t=36

Figure 8: Section 4.4, modes $w^0_{2,1}$ and $w^0_{1,1}$. Snaphshots of the numerical solutions for actin $a(x,t)$, myosin $m(x,t)$ and displacement $u(x,t)$ at times $t = 0, 1, 5, 20, 29, 36$. The cell expands and contracts twice, this can be seen more clearly in Figure 10. The concentration of myosin inside the sphere is shown in Figure 9. (Colour version online).

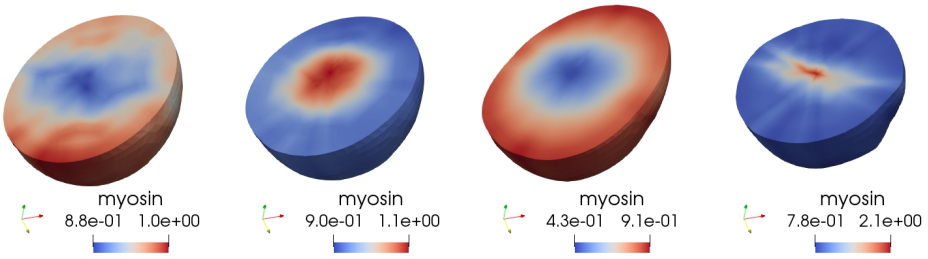

(a) t=5 (b) t=20 (c) t=29 (d) t=36

Figure 9: Graphical representations of the numerical solutions for myosin in Section 4.4 and Figure 8, with a cut-through to see the behaviour in the bulk (interior of the cell). When the cell is expanded the concentration is highest at the edge and later when it is contracted it is largest at the centre. This is also seen in a similar way for the actin concentration. (Colour version online).

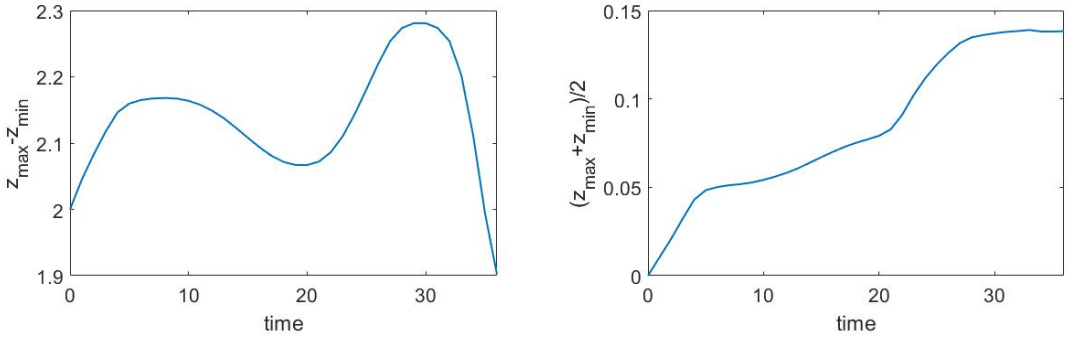

(a) Length of cell in z-direction (b) Translation the centre of the cell in z-direction

Figure 10: Plots to illustrate how the cell expands, contracts and translates in Figure 8. (Example 4.4). (Colour version online).

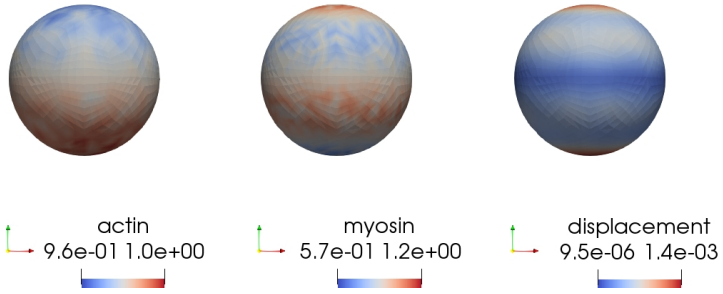

(a) t=0.1

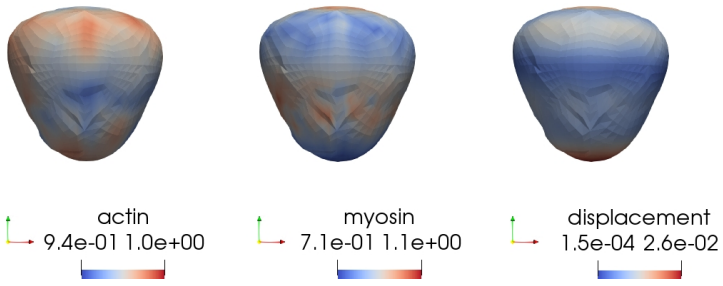

(b) t=2

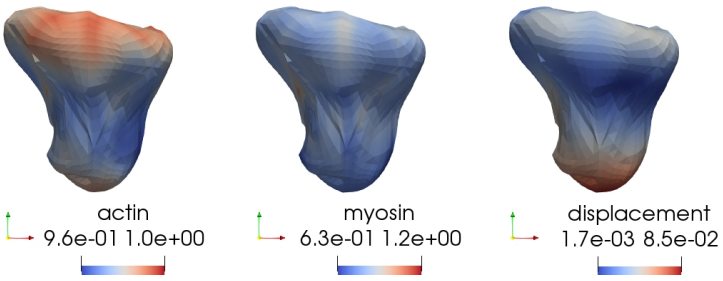

(c) t=7.1

Figure 11: Section 4.5, modes $w^1_{1,1}$ and $w^0_{3,1}$. Snaphshots for the numerical solutions for actin $a(x,t)$, myosin $m(x,t)$ and displacement $u(x,t)$ at times $t = 1, 20, 71$. There is contraction in areas of high myosin, actin accumulates in areas of high curvature and the cell protrudes where there is high actin concentration. The cell deforms to form pseudopods. (Colour version online).

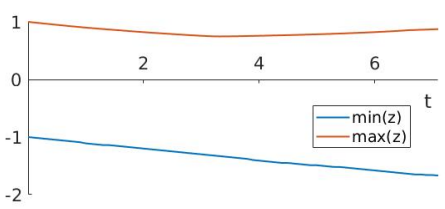

(a) Bounds on z

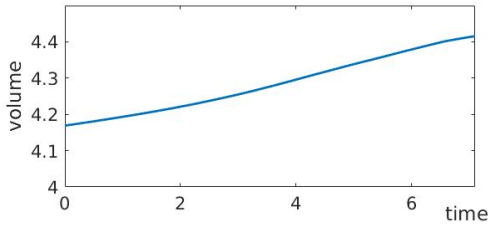

(b) Volume of the cell

Figure 12: Plotting of the range demonstrates that there is a translation followed an expansion in the z-direction. The cell is also being squeezed in the x- and y-direction so we do not observe a significant volume increase (see Example 4.5 and Figure 11). (Colour version online).

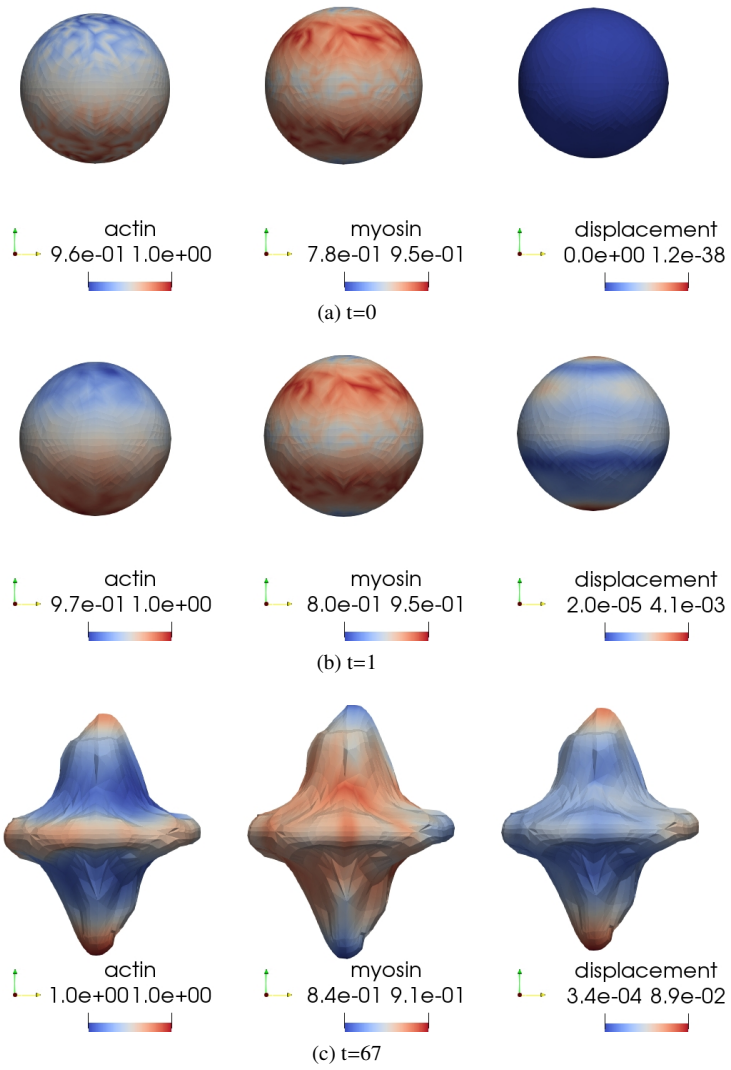

Figure 13: Section 4.6, modes $w^1_{1,1}$ and $w^0_{4,1}$. Snaphshots for the numerical solutions for actin $a(x,t)$, myosin $m(x,t)$ and displacement $u(x,t)$ at times $t = 0, 1, 67$. We see protrusions in a similar way to in Figure 11 but in two directions. The cell deforms to form pseudopods. (Colour version online).

For illustrative purposes, in Figure 14 we plot the L_2-norm of the differences between successive numerical solutions in the case of the full mechanobiochemical model with parameters and initial conditions as in Section 4.4. We see an increase (or decrease) in the L_2 norm when the rate of deformation is accelerating (or decelerating) respectively. The qualitative changes in the L_2 norms are similar, but the changes in myosin and displacement appear slightly later than actin. It must be noted that these norms are not associated with error analysis for the convergence of the model to a steady state. The mechanobiochemical model posed on growing domains does not render itself amenable to numerical analysis due to the complex nature of the model. Here, we are simply post-processing the discrete L_2 norm of the computed numerical solutions.

The mechanobiochemical model is able to generate large cell deformations which in some cases can result in the cell being significantly deformed such that the mesh regularity (Delaunay triangulation criteria) is violated. In our computational software package, *deal.ii*, there are implicit measures for mesh regularity and the numerical computations are terminated once these measures are violated and the stopping criterial is subject to these measures. In future studies, one way to address this issue is to implement adaptive re-meshing strategies to allow the mesh to adapt to large deformations giving rise to long term dynamics of the cell deformation. Equally important, adding a

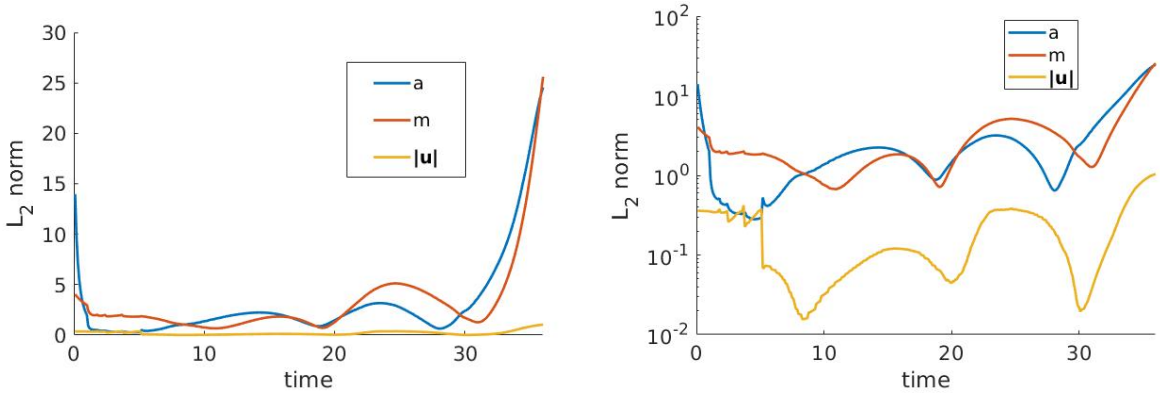

(a) linear scale

(b) log scale

Figure 14: Plot of the L_2 norm of difference between successive solutions for the example shown in Figure 8. There is an initial decrease due to diffusion, increases when the deformation is accelerating and decreases as deformation decelerates. The large error at the end is due to the mesh becoming very deformed and breaking. (Colour version online).

volume constraint term to the model might also prevent large expansions or contractions (see [27, 46, 82] for typical examples). These observations form part of our future studies.

5. Conclusion

Our model balances elasticity, viscosity, contractility and pressure within a linear mechanics framework to model cell migration and deformation. Connected to this are two reaction-diffusion equations for the concentrations of F-actin and bound myosin. Unlike the previous study on which our model is inspired by, (that of George [34]), we have substantially extended the previous model to include two key contributions: (i) we have generalised the model from two to three dimensions, and (ii) we have added a second reaction-diffusion model describing the spatiotemporal dynamics of myosin. Furthermore, our computational framework is developed on a completely different finite element software package, we used the software library *deal.II* [6] to implement the moving grid finite element method. The key difference between this software and the previously used *ALBERTA* [74] is that the elements are hexahedra rather than tetrahedra. The implementation is therefore different but we were able to appropriately replicate the previous results by George [34] of cytomechanical model on a unit two dimensional disk (results not shown) and therefore allows us to validate the numerical methodology. Once this new implementation was verified we extended the model substantially in two ways as noted above. Unlike previous studies of this modelling framework, for the first time, we considered a second reaction-diffusion model to describe how myosin interacts with actin and how it contributes to cell contraction during 3D cell migration. In the absence of experimental observations, we postulated hypothetical reaction kinetics describing the interaction between actin and myosin. As a first step in understanding model solution behaviour in three dimensions of the full model, linear stability analysis close to bifurcation points was carried out and appropriate key parameters identified. A moving grid finite element method was implemented in multi-dimensions using piecewise bilinear shape functions.

Our numerical simulations show that the model extends naturally to three dimensions and that the addition of myosin allows for symmetries to be broken and more striking deformations to emerge. In summary the main numerical results are:

- There is outward movement in areas with high actin concentration, and conversely where there is high curvature, high actin concentration is observed.
- This outward movement due to actin concentration is halted in areas with high myosin concentration. Additionally, if there is low actin and high myosin, we can see negative curvature (Figures 6(d), 11(c) and 13(c)).

- Identifying bifurcation parameters is more complicated than in previous models but the effects of parameter variations can still be observed. The contractility due to myosin, c, strongly effects the speed of the deformation while the reaction constants k_a, k_{ma} and k_{am}, and the diffusion coefficients D_a and D_m play an important part in which eigenmode of the actin and myosin concentrations will be isolated and subsequently formed for the full model. It is not as possible to isolate single modes just by picking parameter values, however, choosing initial conditions as a random number multiplied by the eigenfunction means it is possible to choose modes.
- Several examples show cell translations with small deformations (Figures 8 and 11).
- Initial conditions are a highly significant factor for the progression of the numerical solutions.

Modelling 3D cell migration is an emerging research area where mechanical properties and biochemical processes can now be studied simultaneously due to the recent developments in computational software packages as well as advances in experimental data acquisition and computational power. In this study, we have demonstrated that a reaction-diffusion system for actin and myosin concentrations can give rise to symmetry breaking driven by the displacements of the actin-network which satisfy a mechanical force balance equation. This interplay between continuum mechanics and biochemistry drives cell polarisation from a uniform patterned state. In some cases, the numerical results exhibited are in qualitative agreement with experimental observations. For instance, Example 4.4 illustrates repeated expansion and contraction which has been observed in migrating cells [31, 61, 85]. Previous versions of this model were designed to compare to fibroblast cells, collaborations with experimentalists will be important to determine key parameter values and to see if the model performs in a quantitatively and qualitatively similar way to experimental data in 3D for fibroblast cells as well as for other types of cells.

5.1. Limitations and future directions

We have presented a minimal model by taking into account only linear elasticity theory, coupled with nonlinear stress tensors driven by molecular species, actin and myosin. A natural extension is to study nonlinear mechanics, including nonlinear statistical mechanics to understand the limitations of linear mechanics compared to the nonlinear model. This will also require detailed knowledge of the experimental observations on which to build the nonlinear model.

The modelling and computational framework presented in this article can be readily adapted or extended to consider new experimentally-driven reaction kinetics between actin and myosin or interactions between three or more molecular species, for example, studies using actin, myosin, GEF, Rho, Rac and CDC42 could be productive [39, 42, 60, 76].

Our model considers only the internal workings of the cell and the effect this has on cell movement. In vivo, and in other models it is often assumed that external factors are a driving force in migration. Therefore this framework could be extended to include adhesions and interactions with other cells, obstacles or the extracellular matrix. Since adhesions occur at the cell cortex or membrane/surface, a bulk-surface modelling framework would be a natural candidate approach [46, 28, 48, 65, 22, 15]. Alternatively, as an experiment, different boundary conditions could be considered whereby these boundary conditions are driven by outside forces such as those from movable obstacles or cel-to-cell interactions.

In the current and previous models, cell volume conservation is not maintained. While in most examples, volume change in not significant, the introduction of a mechanism for volume conservation or constraint would help rule out unrealistic large changes in volume [27, 46, 82]. Other useful extensions of the model could use or formulate re-meshing strategies, to avoid distorted cells in highly deformed domains.

A natural extension of this work involves fitting the model to experimental data, in the case that such data exists in the appropriate form. One such approach is to use for example parameter identification [56] or parameter inference [16] for the full mechanobiochemical model. This latter approach will not only provide ranges for the parameters, it will also provide distributions for the parameters, thereby giving much more information about the parameters. The application of such an inverse parameter inference approach is largely missing in current studies of this nature.

Appendix A. Linear stability analysis

In the model from [34], the reaction-diffusion equation alone could not cause patterning . Without the flow term, the prescribed reactions meant the concentration of actin would always return to the homogeneous steady state of $a = a_c$. In our case we have two coupled reaction-diffusion equations which are well known to induce patterning in certain cases.

We perform non-dimensionalisation to reduce parameters and simplify calculations. It also allows the reaction-diffusion equations to take the form necessary to use the standard conditions for diffusion driven instability. This is investigated in detail in [57]. We choose the nondimensionalised parameters:

$$\begin{cases} \tilde{t} = \frac{L^2}{D_a} t, \qquad \tilde{a} = \frac{a}{a_c} = a, \qquad \tilde{m} = \frac{m}{m_c} = m, \qquad d = \frac{D_m}{D_a}, \qquad \tilde{K} = \frac{K}{a_c}, \\ \gamma = \frac{L^2 k_a}{D_a}, \qquad \tilde{k_{ma}} = \frac{k_{ma}}{k_a}, \qquad \tilde{k_{am}} = \frac{k_{am}}{k_a}, \qquad \tilde{k_m} = \frac{k_m}{k_a}, \qquad \tilde{\Delta} = L^2 \Delta, \\ \tilde{\nabla} = L\nabla, \quad \tilde{\mathbf{u}} = \frac{\mathbf{u}}{L}, \quad \tilde{\phi} = \phi, \quad \tilde{\boldsymbol{\varepsilon}} = \boldsymbol{\varepsilon}, \quad \tilde{p} = p\frac{1+\nu}{E}, \\ \tilde{\boldsymbol{\beta}} = \frac{\beta L}{D_a}, \qquad \tilde{a}_{sat} = \frac{a_{sat}}{a_c}, \qquad \tilde{\psi} = \psi a_c^2 \frac{1+\nu}{E} \qquad \tilde{\mu}_i = \frac{\mu_i D_a (1+\nu)}{E L^2}. \end{cases} \tag{A.1}$$

In the above, L is the typical radius of a cell. Substituting appropriately and carrying out algebraic manipulations leads to the following non-dimensionalised system (for general kinetics)

$$\tilde{\nabla} \cdot \left[(\tilde{\mu}_1 \tilde{\boldsymbol{\varepsilon}}_t + \mu_2 \tilde{\phi}_t \mathbf{I}) + (\tilde{\boldsymbol{\varepsilon}} + \nu' \tilde{\phi} \mathbf{I}) + \sigma(\tilde{a}) \mathbf{I} + \tilde{c} \tilde{m} \mathbf{I} + \frac{\tilde{p}(\tilde{a})}{1 + \tilde{\phi}} \mathbf{I} \right] = 0 \tag{A.2a}$$

$$\frac{\partial \tilde{a}}{\partial \tilde{t}} + \tilde{\nabla} \cdot (\tilde{a} \tilde{\boldsymbol{\beta}}) - \tilde{\Delta} \tilde{a} - \gamma f(\tilde{a}, \tilde{m}) = 0 \tag{A.2b}$$

$$\frac{\partial \tilde{m}}{\partial \tilde{t}} + \tilde{\nabla} \cdot (\tilde{m} \tilde{\boldsymbol{\beta}}) - d \tilde{\Delta} \tilde{m} - \gamma g(\tilde{a}, \tilde{m}) = 0. \tag{A.2c}$$

where $\sigma(\tilde{a}) = \tilde{\psi} \tilde{a}^2 e^{-\tilde{a}/\tilde{a}_{sat}}$, $\nu' = \frac{\nu}{1-2\nu}$ and $\tilde{p}(\tilde{a}) = \tilde{p}(1 + \frac{2}{\pi}\delta(l) \arctan \tilde{a})$. f and g have been nondimensionalised and we choose only functions such that system has a steady state at $(a_s, m_s, \mathbf{u}_s) = (1, 1, \mathbf{0})$. Given small variations $\hat{a}, \hat{m}$ and $\hat{\mathbf{u}}$, consider the perturbation from the steady state $\tilde{a} = a_s + \hat{a} = 1 + \hat{a}$, $\tilde{m} = m_s + \hat{m} = 1 + \hat{m}$, $\tilde{\mathbf{u}} = \mathbf{u}_s + \hat{\mathbf{u}} = \hat{\mathbf{u}}$. This results in the linear system

$$\tilde{\nabla} \cdot \left[(\tilde{\mu}_1 \hat{\boldsymbol{\varepsilon}}_t + \mu_2 \hat{\phi}_t \mathbf{I}) + (\hat{\boldsymbol{\varepsilon}} + \nu' \hat{\phi} \mathbf{I}) + \hat{a} \sigma'(1) \mathbf{I} + c \hat{m} \mathbf{I} + \tilde{p}(1 - \hat{\phi}) \mathbf{I} + \tilde{p} \frac{2}{\pi} \delta(l) \hat{a} \mathbf{I} \right] = \mathbf{0}, \tag{A.3a}$$

$$\frac{\partial \hat{a}}{\partial \tilde{t}} + \tilde{\nabla} \cdot (\hat{\beta}) - \tilde{\Delta} \hat{a} - f_a \hat{a} - f_m \hat{m} = 0, \tag{A.3b}$$

$$\frac{\partial \hat{m}}{\partial \tilde{t}} + \tilde{\nabla} \cdot (\hat{\beta}) - d \tilde{\Delta} \hat{m} - g_a \hat{a} - g_m \hat{m} = 0. \tag{A.3c}$$

We now look for solutions of the form

$$\hat{a}(\mathbf{x}, t) = a^* e^{\lambda t + i \mathbf{k} \cdot \mathbf{x}}, \ \hat{m}(\mathbf{x}, t) = m^* e^{\lambda t + i \mathbf{k} \cdot \mathbf{x}} \text{ and } \hat{\mathbf{u}}(\mathbf{x}, t) = \mathbf{u}^* e^{\lambda t + i \mathbf{k} \cdot \mathbf{x}}, \tag{A.4}$$

where λ is the growth rate, $\mathbf{k}$ is the wave vector, and a^*, m^* and $\mathbf{u}^*$ are small amplitudes. We require solutions to be

non-trivial and so we obtain the stability matrix

$$\begin{vmatrix} \lambda + k^2 - \gamma f_a & -\gamma f_m & \lambda ik \\ -\gamma g_a & \lambda + dk^2 - \gamma g_m & \lambda ik \\ -ik\sigma'(1) - ik\tilde{p}\frac{2}{\pi}\delta(l) & -cik & \tilde{\mu}k^2\lambda + k^2(1+\nu') - \tilde{p}k^2 \end{vmatrix} = 0, \text{ where } k = |\mathbf{k}| \tag{A.5a}$$

$$\implies (h(\lambda) :=)\mu\lambda^3 + a(k^2)\lambda^2 + b(k^2)\lambda + c(k^2) = 0, \tag{A.5b}$$

$$\text{where } a(k^2) = k^2(1+d) - \gamma(f_a + g_m) + 1 + \nu' - p - c - (\sigma'(1) + \tilde{p}\frac{2}{\pi}\delta(l)), \tag{A.5c}$$

$$b(k^2) = \tilde{\mu}(k^2 - \gamma f_a)(dk^2 - \gamma g_m) + (1 + \nu' + p)(k^2(1+d) - \gamma(f_a + g_m)) \tag{A.5d}$$

$$-c(k^2 + \gamma(-f_a + g_a)) + (\sigma'(1) + \tilde{p}\frac{2}{\pi}\delta(l))(\gamma(f_m + g_m) - dk^2) - \gamma^2\tilde{\mu}f_m g_a, \tag{A.5e}$$

$$\text{and } c(k^2) = (1 + \nu' + p)\left((k^2 - \gamma f_a)(dk^2 - \gamma g_m) - \gamma^2 f_m g_a\right). \tag{A.5f}$$

Thus $h(\lambda) = 0$ (A.5b) is our dispersal relation and we are concerned with the solution λ. There will be instability when $\text{Re}(\lambda) > 0$. We exploit this relation to isolate particular patterns/modes. The unstable modes will correspond to the eigenfunctions of the Laplacian on the sphere and k^2 the associated eigenvalues.

Appendix A.1. Eigenvalues and eigenfunctions of the Laplacian in the bulk of the unit sphere

The eigenvalues on the unit sphere $\mathbf{\Omega}_0 = \{(x, y, z) : x^2 + y^2 + z^2 \leq 1\}$ (with homogeneous Neumann boundary condition) are well known and are obtained using separation of variables [4, 55]. There are an infinite number of discrete solutions of the form

$$w^m_{l,n}(r, \theta, \phi) = A^m_{l,n} J_{l+\frac{1}{2}}(j'_{l+\frac{1}{2},n} r) e^{im\phi} P^m_l(\cos\theta), \tag{A.6}$$

where l, m, n are all integers such that $|m| \leq l \leq n$, $A^m_{l,n}$ are constants, $J_\alpha(x)$ is a Bessel function of the first kind, i.e. $J_\alpha(x) = \sum_{j=0}^{\infty} \frac{(-1)^j}{j!\Gamma(1+j+\alpha)} \left(\frac{x}{2}\right)^{2j+\alpha}$ with $\Gamma(n) = (n-1)!$, $P^m_l(x)$ are associated Legendre polynomials and $j'_{l+\frac{1}{2},n}$ are zeros of the differential of the spherical Bessel function. We convert eigenfunctions to cartesian coordinates in oder to compare more easily with mechanobiochemical model solutions. We can find the eigenvalues $k^2_{l,n} = (j'_{l+\frac{1}{2},n})^2$ numerically. It follows that for each eigenvalue $\lambda_{l,n} = k^2_{l,n}$ there are $2l + 1$ possible eigenfunctions. Figure 1 shows the eigenfunctions for some selected values of l, m and n. The wave numbers are discrete.

Appendix A.2. Parameter selection

The conditions on the positivity of the roots of (A.5b) are numerous and the coefficients of the polynomial are burdensome. Therefore, we numerically find these roots and observe the real and imaginary parts.

We found that contractility due to myosin (c), and due to actin (ψ) are particularly significant for finding unstable wavenumbers. In Figure A.15a we plot the real and imaginary parts of the solution against k^2 for three different values of c. We can see that when wavenumbers k^2 are less than ~ 12, then $\text{Re}(\lambda) > 0$ for the three values of c, therefore the wavenumbers will be unstable. Additionally these wavenumbers will be oscillatory for $c = 10$. There are also regions of Hopf instability and oscillatory instability for all the three values of c. In Figure A.15b we fix other parameters and vary ψ to see that, just like in [34] higher values of ψ mean higher wavenumbers can be excited.

Acknowledgements

This work (LM) was supported by an EPSRC Doctoral Training Centre Studentship through the University of Sussex. AM acknowledges support from the Leverhulme Trust Research Project Grant (RPG-2014-149). This work (AM) has received funding from the European Union Horizon 2020 research and innovation programme under the Marie Sklodowska-Curie grant agreement (No 642866). AM is a Royal Society Wolfson Research Merit Award Holder, generously supported by the Wolfson Foundation. LM acknowledges the support from the University of Sussex ITS for computational purposes. AM is a Visiting Scholar to the Department of Mathematics, University of Johannesburg, South Africa.

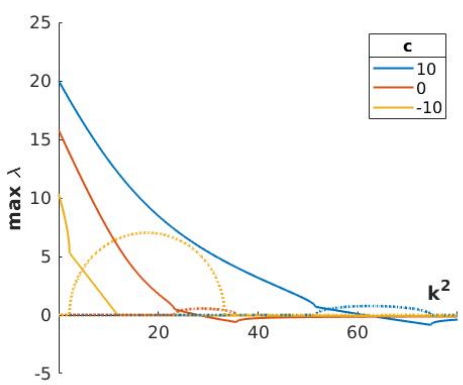

(a) Plot to show maximum real (solid line) and imaginary (dotted line) parts of the solution to the dispersal relation. The three colours are denote three different values of c. In this case we fix $\psi = 100$

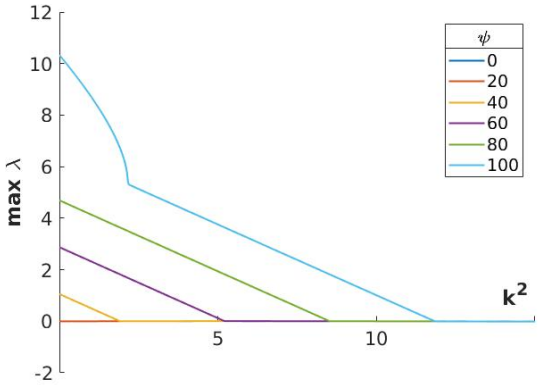

(b) Plot to show maximum real part of λ as ψ is varied. In this case we fix $c = -10$

Figure A.15: The effects of varying parameters on behaviour of solutions.

References

[1] DJ Acheson. *Elementary fluid dynamics: Oxford applied mathematics and computing science series*. Oxford University Press, Oxford, 1990.

[2] R Aguilar-Cuenca, A Juanes-García, and M Vicente-Manzanares. Myosin ii in mechanotransduction: master and commander of cell migration, morphogenesis, and cancer. *Cellular and molecular life sciences*, 71(3):479–492, 2014.

[3] W Alt and RT Tranquillo. Basic morphogenetic system modeling shape changes of migrating cells: How to explain fluctuating lamellipodial dynamics. *Journal of Biological Systems*, 3(04):905–916, 1995.

[4] G Arfken, H Weber, and F Harris. *Mathematical methods for physicists*. Elsevier, Amsterdam, 2013.

[5] MJ Baines. *Moving finite elements, Monographs on Numerical Analysis*. Clarendon Press, Oxford, 1994.

[6] W Bangerth, T Heister, L Heltai, G Kanschat, M Kronbichler, M Maier, and B Turcksin. The deal.ii library, version 8.3. *Archive of Numerical Software*, 4(100):1–11, 2016. ISSN 2197-8263. doi: 10.11588/ans.2016.100.23122.

[7] AR Bausch, F Ziemann, AA Boulbitch, K Jacobson, and E Sackmann. Local measurements of viscoelastic parameters of adherent cell surfaces by magnetic bead microrheometry. *Biophysical journal*, 75(4):2038–2049, 1998.

[8] PM Bendix, GH Koenderink, D Cuvelier, Z Dogic, BN Koeleman, WM Brieher, CM Field, L Mahadevan, and DA Weitz. A quantitative analysis of contractility in active cytoskeletal protein networks. *Biophysical journal*, 94(8):3126–3136, 2008.

[9] A Bertram. *Elasticity and plasticity of large deformations*. Springer, 2012.

[10] Konstantinos N Blazakis. *Computational methods for investigating cell motility with applications to neutrophil cell migration*. PhD thesis, University of Sussex, 2015.

[11] D Bottino and L Fauci. A computational model of ameboid deformation and locomotion. *European Biophysics Journal*, 27(5):532–539, Aug 1998. doi: 10.1007/s002490050163. URL https://doi.org/10.1007/s002490050163.

[12] D Bottino, A Mogilner, T Roberts, M Stewart, and G Oster. How nematode sperm crawl. *Journal of cell science*, 115(2):367–384, 2002.

[13] D Bray. *Cell movements: from molecules to motility*. Garland Science, 2001.

[14] V Brinkmann, U Reichard, C Goosmann, B Fauler, Y Uhlemann, DS Weiss, Y Weinrauch, and A Zychlinsky. Neutrophil extracellular traps kill bacteria. *science*, 303(5663):1532–1535, 2004.

[15] EJ Campbell and P Bagchi. A computational model of amoeboid cell motility in the presence of obstacles. *Soft matter*, 2018.

[16] E Campillo-Funollet, C Venkataraman, and A Madzvamuse. Bayesian parameter identification for turing systems on stationary and evolving domains. *Bulletin of mathematical biology*, 81(1):81–104, 2019.

[17] AR Carotenuto, A Cutolo, A Petrillo, R Fusco, C Arra, M Sansone, D Larobina, L Cardoso, and M Fraldi. Growth and in vivo stresses traced through tumor mechanics enriched with predator-prey cells dynamics. *Journal of the mechanical behavior of biomedical materials*, 86:55–70, 2018.

[18] P Chatzipantelidis, Z Horváth, and V Thomée. On preservation of positivity in some finite element methods for the heat equation. *Computational Methods in Applied Mathematics*, 15(4):417–437, 2015.

[19] J Chen, J Irianto, S Inamdar, P Pravincumar, DA Lee, Dan L Bader, and MM Knight. Cell mechanics, structure, and function are regulated by the stiffness of the three-dimensional microenvironment. *Biophysical journal*, 103(6):1188–1197, 2012.

[20] J Condeelis and JE Segall. Intravital imaging of cell movement in tumours. *Nature Reviews Cancer*, 3(12):921, 2003.

[21] GM Cooper. *The Cell: A Molecular Approach. 2nd edition.* Sinauer Associates, Sunderland (MA), 2000.

[22] D Cusseddu, L Edelstein-Keshet, JA Mackenzie, S Portet, and A Madzvamuse. A coupled bulk-surface model for cell polarisation. *Journal of Theoretical Biology*, 2018.

[23] VS Deshpande, RM McMeeking, and AG Evans. A bio-chemo-mechanical model for cell contractility. *Proceedings of the National Academy of Sciences*, 103(38):14015–14020, 2006.
[24] EH Dill. *Continuum Mechanics: Elasticity, Plasticity, Viscoelasticity*. CRC press, Germany, 2006.
[25] A Dreher, IS Aranson, and K Kruse. Spiral actin-polymerization waves can generate amoeboidal cell crawling. *New Journal of Physics*, 16 (5):055007, 2014.
[26] G Dziuk and CM Elliott. Finite elements on evolving surfaces. *IMA journal of numerical analysis*, 27(2):262–292, 2007.
[27] C Elliott, B Stinner, and C Venkataraman. Modelling cell motility and chemotaxis with evolving surface finite elements. *J. Roy. Soc. Interface*, 9(76):3027–3044, 2012.
[28] CM Elliott and T Ranner. Finite element analysis for a coupled bulk–surface partial differential equation. *IMA Journal of Numerical Analysis*, 33(2):377–402, 2013.
[29] M Fraldi and AR Carotenuto. Cells competition in tumor growth poroelasticity. *Journal of the Mechanics and Physics of Solids*, 112:345–367, 2018.
[30] M Fraldi, A Cugno, AR Carotenuto, A Cutolo, NM Pugno, and L Deseri. Small-on-large fractional derivative–based single-cell model incorporating cytoskeleton prestretch. *Journal of Engineering Mechanics*, 143(5):D4016009, 2016.
[31] P Friedl. Prespecification and plasticity: shifting mechanisms of cell migration. *Current opinion in cell biology*, 16(1):14–23, 2004.
[32] P Friedl and D Gilmour. Collective cell migration in morphogenesis, regeneration and cancer. *Nature reviews Molecular cell biology*, 10(7): 445–457, 2009.
[33] M Frittelli, A Madzvamuse, I Sgura, and C Venkataraman. Lumped finite elements for reaction–cross-diffusion systems on stationary surfaces. *Computers & Mathematics with Applications*, 74(12):3008–3023, 2017.
[34] UZ George. *A numerical approach to studying cell dynamics*. PhD thesis, University of Sussex, 2012.
[35] UZ George, A Stéphanou, and A Madzvamuse. Mathematical modelling and numerical simulations of actin dynamics in the eukaryotic cell. *Journal of mathematical biology*, pages 1–47, 2013.
[36] Christophe Geuzaine and Jean-François Remacle. Gmsh: A 3-d finite element mesh generator with built-in pre-and post-processing facilities. *International journal for numerical methods in engineering*, 79(11):1309–1331, 2009.
[37] E Gladilin, A Micoulet, B Hosseini, K Rohr, J Spatz, and R Eils. 3d finite element analysis of uniaxial cell stretching: from image to insight. *Physical biology*, 4(2):104, 2007.
[38] ME Gracheva and HG Othmer. A continuum model of motility in ameboid cells. *Bulletin of mathematical biology*, 66(1):167–193, 2004.
[39] A Hall. Rho gtpases and the actin cytoskeleton. *Science*, 279(5350):509–514, 1998.
[40] MR Hestenes and E Stiefel. Methods of conjugate gradients for solving linear systems. *J Res Nat Bur Stand*, 49(6):409–436, 1952.
[41] N Hodge and P Papadopoulos. Continuum modeling and numerical simulation of cell motility. *Journal of mathematical biology*, 64(7): 1253–1279, 2012.
[42] WR Holmes, AE Golding, WM Bement, and L Edelstein-Keshet. A mathematical model of gtpase pattern formation during single-cell wound repair. *Interface focus*, 6(5):20160032, 2016.
[43] O Lakkis, A Madzvamuse, and C Venkataraman. Implicit–explicit timestepping with finite element approximation of reaction–diffusion systems on evolving domains. *SIAM Journal on Numerical Analysis*, 51(4):2309–2330, 2013.
[44] MA Lewis and JD Murray. Analysis of stable two-dimensional patterns in contractile cytogel. *Journal of Nonlinear Science*, 1(3):289–311, 1991.
[45] C Lu, W Huang, and J Qiu. Maximum principle in linear finite element approximations of anisotropic diffusion–convection–reaction problems. *Numerische Mathematik*, 127(3):515–537, 2014.
[46] G MacDonald, JA Mackenzie, M Nolan, and RH Insall. A computational method for the coupled solution of reaction–diffusion equations on evolving domains and manifolds: Application to a model of cell migration and chemotaxis. *Journal of computational physics*, 309:207–226, 2016.
[47] A Madzvamuse. Time-stepping schemes for moving grid finite elements applied to reaction–diffusion systems on fixed and growing domains. *J Comput Phys*, 214(1):239–263, 2006.
[48] A Madzvamuse and A Chung. The bulk-surface finite element method for reaction–diffusion systems on stationary volumes. *Finite Elem Anal Des*, 108:9–21, 2016.
[49] A Madzvamuse, A Wathen, and P Maini. A moving grid finite element method applied to a model biological pattern generator. *J Comput Phys*, 190(2):478–500, 2003.
[50] A Madzvamuse, E Gaffney, and P Maini. Stability analysis of non-autonomous reaction-diffusion systems: the effects of growing domains. *J Math Biol*, 61(1):133–164, 2010.
[51] A Madzvamuse, H Ndakwo, and R Barreira. Cross-diffusion-driven instability for reaction-diffusion systems: analysis and simulations. *J Math Biol*, 70(4):709–743, 2015.
[52] Anotida Madzvamuse and Uduak Zenas George. The moving grid finite element method applied to cell movement and deformation. *Finite Elements in Analysis and Design*, 74:76–92, 2013.
[53] A Manhart, D Oelz, C Schmeiser, and N Sfakianakis. Numerical treatment of the filament-based lamellipodium model (fblm). In *Modeling cellular systems*, pages 141–159. Springer, 2017.
[54] E McEvoy, VS Deshpande, and P McGarry. Transient active force generation and stress fibre remodelling in cells under cyclic loading. *Biomechanics and modeling in mechanobiology*, pages 1–17, 2019.
[55] M Morimoto. *Analytic functionals on the sphere*. American Mathematical Society, Providence, R.I., 1998.
[56] L Murphy, C Venkataraman, and A Madzvamuse. Parameter identification through mode isolation for reaction–diffusion systems on arbitrary geometries. *International Journal of Biomathematics*, 11(04):1850053, 2018.
[57] LR Murphy. *Mathematical studies of a mechanobiochemical model for 3D cell migration*. PhD thesis, University of Sussex, 2018.
[58] M Murrell, PW Oakes, M Lenz, and ML Gardel. Forcing cells into shape: the mechanics of actomyosin contractility. *Nature Reviews Molecular Cell Biology*, 16(8):486–498, 2015.
[59] MP Neilson, JA Mackenzie, SD Webb, and RH Insall. Modeling cell movement and chemotaxis using pseudopod-based feedback. *SIAM*

Journal on Scientific Computing, 33(3):1035–1057, 2011.
[60] CD Nobes and A Hall. Rho, rac, and cdc42 gtpases regulate the assembly of multimolecular focal complexes associated with actin stress fibers, lamellipodia, and filopodia. *Cell*, 81(1):53–62, 1995.
[61] M Noguchi, K Sumiyama, and M Morimoto. Directed migration of pulmonary neuroendocrine cells toward airway branches organizes the stereotypic location of neuroepithelial bodies. *Cell reports*, 13(12):2679–2686, 2015.
[62] GF Oster, JD Murray, and GM Odell. Formation of microvilli. Technical report, Los Alamos National Lab., NM (USA), 1985.
[63] C Pozrikidis. Numerical simulation of cell motion in tube flow. *Annals of Biomedical Engineering*, 33(2):165–178, 2005.
[64] WH Press, SA Teukolsky, WT Vetterling, and BP Flannery. *Numerical recipes 3rd edition: The art of scientific computing*. Cambridge university press, 2007.
[65] A Rätz and M Röger. Symmetry breaking in a bulk–surface reaction–diffusion model for signalling networks. *Nonlinearity*, 27(8):1805, 2014.
[66] JN Reddy. *An introduction to the finite element method.* McGraw-Hill, New York, 1993.
[67] P Rørth. Collective cell migration. *Annual review of cell and developmental*, 25:407–429, 2009.
[68] M Rossi, G Cicconofri, A Beran, G Noselli, and A DeSimone. Kinematics of flagellar swimming in euglena gracilis: Helical trajectories and flagellar shapes. *Proceedings of the National Academy of Sciences*, 114(50):13085–13090, 2017.
[69] B Rubinstein, K Jacobson, and A Mogilner. Multiscale two-dimensional modeling of a motile simple-shaped cell. *Multiscale Modeling & Simulation*, 3(2):413–439, 2005.
[70] B Rubinstein, MF Fournier, K Jacobson, AB Verkhovsky, and A Mogilner. Actin-myosin viscoelastic flow in the keratocyte lamellipod. *Biophysical journal*, 97(7):1853–1863, 2009.
[71] S Ruuth. Implicit-explicit methods for reaction-diffusion problems in pattern formation. *J Math Biol*, 34(2):148–176, 1995.
[72] Y Saad and MH Schultz. Gmres: A generalized minimal residual algorithm for solving nonsymmetric linear systems. *SIAM Journal on scientific and statistical computing*, 7(3):856–869, 1986.
[73] Y Sakamoto, S Prudhomme, and MH Zaman. Modeling of adhesion, protrusion, and contraction coordination for cell migration simulations. *Journal of mathematical biology*, 68(1-2):267–302, 2014.
[74] A Schmidt, KG Siebert, D Köster, O Kriessl, and CJ Heine. Alberta-an adaptive hierarchical finite element toolbox. *URL http://www. alberta-fem. de*, 2007.
[75] D Shao, H Levine, and W Rappel. Coupling actin flow, adhesion, and morphology in a computational cell motility model. *Proceedings of the National Academy of Sciences*, 109(18):6851–6856, 2012.
[76] CM Simon, EM Vaughan, WM Bement, and L Edelstein-Keshet. Pattern formation of rho gtpases in single cell wound healing. *Molecular biology of the cell*, 24(3):421–432, 2013.
[77] A Stephanou, MAJ Chaplain, and P Tracqui. A mathematical model for the dynamics of large membrane deformations of isolated fibroblasts. *Bulletin of mathematical biology*, 66(5):1119, 2004.
[78] W Strychalski, D Adalsteinsson, and TC Elston. Simulating biochemical signaling networks in complex moving geometries. *SIAM Journal on Scientific Computing*, 32(5):3039–3070, 2010.
[79] M Tozluoğlu, AL Tournier, RP Jenkins, S Hooper, PA Bates, and E Sahai. Matrix geometry determines optimal cancer cell migration strategy and modulates response to interventions. *Nature cell biology*, 15(7):751–762, 2013.
[80] CW Wolgemuth and M Zajac. The moving boundary node method: A level set-based, finite volume algorithm with applications to cell motility. *Journal of computational physics*, 229(19):7287–7308, 2010.
[81] CW Wolgemuth, J Stajic, and A Mogilner. Redundant mechanisms for stable cell locomotion revealed by minimal models. *Biophysical journal*, 101(3):545–553, 2011.
[82] FW Yang, C Venkataraman, V Styles, and A Madzvamuse. A robust and efficient adaptive multigrid solver for the optimal control of phase field formulations of geometric evolution laws. *Communications in Computational Physics*, 21(1):65–92, 2017.
[83] D Yu. *Nonlinear continuum mechanics and Large Inelastic Deformations*. Springer, 2011.
[84] MH Zaman, RD Kamm, P Matsudaira, and DA Lauffenburger. Computational model for cell migration in three-dimensional matrices. *Biophysical journal*, 89(2):1389–1397, 2005.
[85] Jie Zhu and Alex Mogilner. Comparison of cell migration mechanical strategies in three-dimensional matrices: a computational study. *Interface Focus*, 6(5):20160040, 2016.